



Numerical simulation of two-phase flows in complex geometries by using the volume-of-fluid/immersed-boundary method

Xiaosong Sun ^{a,*}, Mikio Sakai ^{b,*}

^a Department of Nuclear Engineering and Management, School of Engineering, The University of Tokyo, 7-3-1 Hongo, Bunkyo-ku, Tokyo 113-8656, Japan

^b Resilience Engineering Research Center, School of Engineering, The University of Tokyo, 7-3-1 Hongo, Bunkyo-ku, Tokyo 113-8656, Japan



HIGHLIGHTS

- We develop a numerical model for simulating two-phase flows in complex geometries.
- The method is based on volume-of-fluid and immersed boundary approaches.
- Our modeling allows for highly complicated wall boundaries and moving bodies.
- A variety of test problems have been performed to validate the present method.
- We also present its application to the simulation of a twin screw kneader.

ARTICLE INFO

Article history:

Received 30 June 2015

Received in revised form

10 September 2015

Accepted 21 September 2015

Available online 9 October 2015

Keywords:

Two-phase flow

Complex geometry

Volume-of-fluid method

Immersed boundary method

ABSTRACT

The numerical modeling of two-phase flows in complex geometries is of special relevance in many scientific and industrial applications. In this paper, we describe a numerical method to perform three-dimensional simulations of such flow problems. This method adopts a volume-of-fluid (VOF) approach to capture and advance the fluid interface, and it integrates the fluid solver with the immersed boundary (IB) modeling of arbitrary-shape walls and moving bodies. The shape and movement of solid geometries are efficiently represented by an auxiliary signed distance function (SDF) with local coordinate transformation. Validation tests have been conducted using the present method, and the computational results are in good agreements with reference solutions and experimental data. We further present its application to the simulation of the air–water flow in a twin screw kneader. Hence, the adequacy and suitability of the present VOF–IB method are shown to successfully simulate complicated two-phase flows interacting with general geometries.

© 2015 Elsevier Ltd. All rights reserved.

1. Introduction

Incompressible two-phase flows interacting with complex geometries and moving bodies are ubiquitous in numerous industrial circumstances. Their applications in chemical engineering include sprays (Davanlou et al., 2015) and jets (Homma et al., 2006; Nabavi et al., 2015) from nozzles, the droplet impingement on walls (Mahulkar et al., 2015), compounding in micro-devices (Santana et al., 2015; Wang et al., 2015), stirred tanks (Solsvik and Jakobsen, 2015), bubble columns (Ma et al., 2015) and high viscosity mixers (Barailler et al., 2006). Efficient, accurate and

robust computation of these flow problems are gaining increasing attentions in recent years.

For practical simulation of those flow problems, there are two major aspects of special concern: the modeling of fluid interface and the modeling of fluid–boundary interaction. In two-phase flows, fluids are separated by a sharp-interface. Among a large variety of numerical models for solving interfacial problems (see (Tryggvason et al., 2011) for an extensive review), the so-called ‘interface capturing’ methods are good choices for predicting the motion of immiscible fluids involving complex fluid interface, large density ratio and general flow conditions. Basically, an interface capturing method follows an Eulerian description of fluid motion and has a fixed Cartesian grid covering the whole fluid domain. On that grid a field variable, viz. the indicator function, is discretized to identify and move the fluid interface. The volume-of-fluid (VOF) method (Hirt and Nichols, 1981) and the level set

* Corresponding authors. Tel./fax: +81 3 5841 6977

E-mail addresses: song@dem.t.u-tokyo.ac.jp (X. Sun), mikio_sakai@n.t.u-tokyo.ac.jp (M. Sakai).

(LS) method (Sussman et al., 1994) are the most famous and successful ones in the interface capturing family. In the VOF method, the volume fraction of one fluid phase in each computational cell is adopted as the color function to distinguish different fluids. A typical procedure in the VOF method contains a geometrical reconstruction and advection of the binary interface using the volume fraction. To this end, several varieties of the VOF algorithm have been proposed, see the comparative studies of (Aniszewski et al., 2014; Gopala and van Wachem, 2008). The VOF method has good properties of volume conservation, but it is difficult to exactly locate the interfacial point and compute the surface tension. The LS method directly stores a signed distance field (i.e. the level set function) whose zero-contour corresponds to the fluid interface. High-order upwind methods for hyperbolic laws can be applied to the LS interface advection (Osher and Fedkiw, 2002) in a straightforward way. However, the LS method is known to suffer from the loss of mass problem (Sussman et al., 1998, 1994). Besides some improvements made individually to the VOF and LS methods, a coupled level set and volume-of-fluid (CLSVOF) method (Sussman and Puckett, 2000) has been proposed to combine their advantages. The applications of those two-phase flow models have been found in bubble dynamics (Van Sint Annaland et al., 2005), gas–liquid heat transport (Deen and Kuipers, 2013), fluidization systems (Ge and Fan, 2006), bubbly (Jain et al., 2014) or particulate (Deen et al., 2006) flows and food filling (Matsumoto et al., 2015).

To model fluid-boundary interaction, the immersed boundary (IB) method is thought to be efficient, which is able to represent non-conforming boundary shapes on fixed computational grids. Compared with traditional body-fitted grids, the IB method is free of the costly gridding procedure and is allowed to have almost unrestricted object motions. In general, existing IB methods could be categorized into two types in respect of the way how the flow field is modified near the immersed boundary. In the ‘continuous forcing’ IB method originated by Peskin (Peskin, 2002, 1977), the immersed interface is represented by distinct Lagrangian points and their actions to the fluid are scattered in surrounding fluid cells. The ‘direct forcing’ IB method (Fadlun et al., 2000) adopts an alternative approach, in which the near-wall velocity given by the interpolation based on local geometry profile is prescribed directly at fluid grids embedding the boundary. (Kajishima and Takiguchi, 2002; Kajishima et al., 2001) proposed a simpler formulation of direct forcing IB method: at the fluid-solid cells, fluid and solid velocities are explicitly mixed by using the local solid volume fraction as a weight factor. This method is efficient and suitable for the situation when a fluid point is interacting with multiple solid objects. Different versions of the IB method have been successfully applied to the numerical simulation of particulate flows (Lin et al., 2011; Uhlmann, 2005), body-induced air flows (Choi et al., 2007), and turbulent flows (Ikeno and Kajishima, 2007; Yang and Balaras, 2006).

In the past, some numerical methods have been proposed for simulating two-phase flows in general geometries by connecting the VOF method and immersed boundary models on fixed grids. (Kleefsman et al., 2005) and (Lin, 2007) developed their own free surface flow solvers ignoring the air phase. In (Jain et al., 2012) and (Lin and Chen, 2013), the Navier-Stokes equation is solved in the whole computational domain so that the gas motion is also taken into consideration. Their solvers are further combined with the IB method and the discrete element method (DEM) (Cundall and Strack, 1979) to simulate wet impact problems. However, the treatment of contact angle boundary condition is not specified in those literatures.

The LS method is also frequently adopted for simulating two-phase flows in complex geometries. (Sussman, 2005, 2001) described a CLSVOF method for multiphase flows with application to ship hydrodynamics. An iterative algorithm extends the LS

function into the solid domain in order to satisfy the contact angle boundary condition without explicitly locating the position of the contact line. (Yang and Stern, 2009) developed the LS/IB method to simulate wave problems. In their study, the density/pressure jump across the gas–liquid interface is treated by using a sharp-interface model. At the solid surface, the LS function is directly modified in a way consistent with linear interface fitting to explicitly prescribe the neutral (90°) contact angle boundary condition. Other numerical studies based on the LS–IB combination include two-dimensional wave-body interaction (Yoon et al., 2013), bubble adherence (Son, 2005), and three-dimensional jet atomization (Arienti and Sussman, 2014).

In this study, we will focus on a novel combination of the VOF method and the IB method for three-dimensional simulations of two-phase flows interacting with complex geometries. Its development is largely motivated by our interest to model some mixing devices used in chemical engineering, which usually have severely distorted free surfaces, complicated shapes and moving parts. In this respect, it is expected that our VOF–IB method can simulate the generality of fluid interfaces and solid boundaries as well as their interactions with ease. Specifically, there are four requirements for solving such flow problems. (a) The fluid interface must be computed accurately while keeping sharp, so that the interfacial motion is properly predicted. (b) The modeling of general geometries shall be efficient and robust for practical computations usually involving multiple parts in movement. (c) Apart from ‘fundamental’ geometries such as cylinders and spheres, we would like to consider some truly complicated ones, e.g. the rotating paddle in a twin screw kneader, for which an effective shape representation is needed. (d) As a unique problem in two-phase flows, the contact angle boundary condition is also to be satisfied on the solid surface of a complex geometry. The originality of the present method lies in the following points.

- First, the THINC/WLIC scheme (Yokoi, 2007) is used for VOF interface reconstruction and advection, which could be implemented in 3D space more easily than traditional PLIC (piecewise linear interface calculation) method (Youngs, 1982) while it is able to capture the fluid interface with comparable accuracy.
- Second, the IB model proposed by (Kajishima et al., 2001) is chosen for calculating fluid-boundary interactions. In comparison with other direct forcing IB formulation with geometrical interpolation, its velocity blending based on a ‘volume-of-solid’ approach provides a straightforward way to handle multiple moving bodies that might come close to each other.
- Third, the wall boundary and moving objects now have a special level set representation which is based on our arbitrary-shape wall boundary model developed in (Shigeto and Sakai, 2013). Not only could primary shapes be modeled but also very complicated ones are able to be imported from computer aided design (CAD) data.
- Last but not least, we propose some simplified treatments to prescribe the neutral contact angle boundary condition for systems involving complex geometries.

We perform tests and provide comparison to analytical solution or experimental data in order to validate the proposed VOF–IB method. We also present its application to gas–liquid flows within a laboratory twin screw kneader as an example involving highly complex geometries and rotating parts. In this way, the proposed VOF–IB solver is shown to be a useful and versatile tool for the prediction of various flow systems.

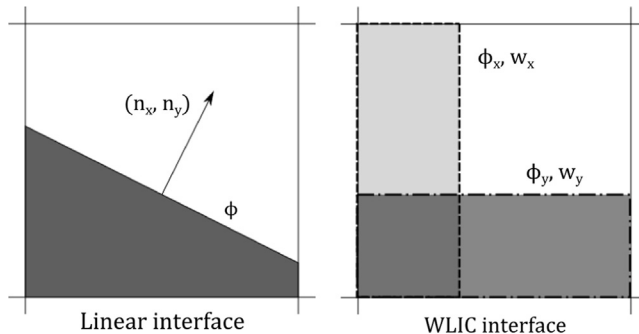


Fig. 1. Schematic diagram of WLIC interface reconstruction.

2. Governing equations

We consider an incompressible Newtonian flow composed of two immiscible fluids confined by solid boundaries. Its motion is governed by the Navier-Stokes equation (modified to reflect the immersed boundary) and the continuity equation:

$$\frac{\partial \mathbf{u}}{\partial t} + \nabla \cdot (\mathbf{u}\mathbf{u}) = -\frac{1}{\rho} \nabla p + \frac{1}{\rho} \nabla \cdot \mu(\nabla \mathbf{u} + \nabla \mathbf{u}^T) - \frac{1}{\rho} \sigma \kappa \delta \mathbf{n} + \mathbf{g} + \mathbf{f}_B \quad (1)$$

$$\nabla \cdot \mathbf{u} = 0 \quad (2)$$

where \mathbf{u} is fluid velocity, ρ is fluid density, μ is dynamic viscosity, p is pressure, σ is coefficient of surface tension, κ is local mean curvature, δ is a delta function non-zero at the interface, \mathbf{n} is the interface normal vector, \mathbf{g} is gravity, and \mathbf{f}_B stands for the external forcing on the fluid due to immersed boundary, whose role is to enforce the condition $\mathbf{u} = \mathbf{u}_B$ with \mathbf{u}_B the boundary velocity. Hence, the terms on the right hand side of the Navier-Stokes Eq. (1) represent the effects of pressure gradient, viscosity, surface tension, gravity and wall boundary, respectively.

The VOF function ϕ is defined as the volume fraction of the 'liquid' phase out of the binary fluid mixture. Its value is 1 in 'liquid', 0 in 'gas', and $0 < \phi < 1$ at the interface. The temporal evolution of the fluid interface can be obtained by solving the passive advection equation:

$$\frac{\partial \phi}{\partial t} + \mathbf{u} \cdot \nabla \phi = 0 \quad (3)$$

Using the VOF function, fluid density ρ and dynamic viscosity μ could be calculated from original physical properties of the liquid and gas phases as follows.

$$\rho(\phi) = \phi \rho_l + (1 - \phi) \rho_g \quad (4)$$

$$\mu(\phi) = \phi \mu_l + (1 - \phi) \mu_g \quad (5)$$

where the subscript *l* and *g* denote liquid and gas phases, respectively.

3. Arbitrary-shaped wall boundary model

The arbitrary-shaped wall boundary model developed in our previous study (Shigeto and Sakai, 2013) is a highly reusable programming module that can provide a signed distance function (SDF) based representation of geometric shapes independent of the application context where it is deployed. The arbitrary-shape wall boundary model and its analogy have already been successfully applied to our previous Lagrangian particle simulations of granular materials (Shigeto and Sakai, 2013) and solid-liquid granular flows (Sun et al., 2014, 2013; Yamada and Sakai, 2013). For the sake of completeness, the basic concept, construction and

utility about the arbitrary-shape wall boundary model is described in this section.

3.1. SDF solid representation and its construction

The solid boundary representation is based on the implicit zero-contour surface defined with a special SDF ψ_B . Following the convention in level set literatures, $\psi_B < 0$ in the region occupied by the solid body. In principle, for a given point we can directly retrieve the shortest distance ψ_B to the solid surface and get the boundary normal vector (pointing outwards from solid region) as

$$\mathbf{n}_B = \frac{\nabla \psi_B}{|\nabla \psi_B|} \quad (6)$$

The present SDF model can also support rigid motions including translation and rotation. A local coordinate is associated with each SDF field to reflect rigid body motion. Coordinate transformation is described by quaternion and get updated every time as translational or rotational motion occurs.

The original solid object is described by a triangular surface mesh, which need not be of high quality, as stretched elements are also allowable as long as no hanging node exists. The construction of ψ_B is equal to finding the minimal distance for the current point among all nodes, edges and elements in the original surface mesh. Its calculation is independently performed on a uniform grid (namely the SDF grid); once calculated, the ψ_B field could be cached for future reuse. When there are N objects, their SDF fields are built and saved separately as $\psi_{B1}, \psi_{B2}, \dots, \psi_{BN}$.

3.2. SDF utility for the fluid solver

As mentioned above, the SDF is kept on auxiliary grids that generally do not coincide with the fluid grid. In our case, the auxiliary grid has a resolution finer than that used in fluid simulation (usually the grid size is a factor > 2 smaller than the fluid grid size). So that from the viewpoint of the fluid solver, the definition of boundary shapes is always sufficiently precise.

At the beginning of each step in the VOF-IB solver, we first transfer the SDF values to the fluid cell (i, j, k) and generate a single boundary profile ψ compatible with multiple solid objects:

$$\psi_{ijk} = \min(\psi_{B1}(\mathbf{x}_{ijk}), \psi_{B2}(\mathbf{x}_{ijk}), \dots, \psi_{BN}(\mathbf{x}_{ijk})). \quad (7)$$

The combining operation by taking their minimum has two reasons: (a) the resulting SDF field will give the closest distance to the wall in the fluid and (b) any point with a negative SDF value must belong to the corresponding solid domain.

From the SDF model, we can also obtain the solid volume fraction α_{ijk} which is important for the IB treatment in Section 5.2. In this study, each fluid cell is refined to $8 \times 8 \times 8$ finer volumes of which the SDF signs at the centers are checked. The volume occupied by the solid is then approximated by the ratio of non-positive fine volumes out of all subdivisions.

4. WLIC VOF interface advection

In the THINC/WLIC VOF scheme, piecewise constant reconstruction of the interface similar to the SLIC (simple line interface calculation) (Noh and Woodward, 1976) is carried out along *x*, *y*, and *z*-coordinates, respectively. All these three flat interfaces are used to determine the upwind, geometrical flux F_m passing through the corresponding cell face,

$$F_m = \int_{u\Delta t} \varphi dV \text{ with } 1 \leq m \leq N_{\text{dim}}. \quad (8)$$

A weighted average of the resulting fluxes is calculated taking in account the local surface orientation, i.e. $F = \sum w_m F_m$. Fig. 1 provides 2D schematics and weight functions for clarity.

To advance the fluid interface in time, the VOF advection Eq. (3) is written in the form

$$\frac{\partial \varphi}{\partial t} + \nabla \cdot (\mathbf{u}\varphi) - (\nabla \cdot \mathbf{u})\varphi = 0 \quad (9)$$

Then the multidimensional equation is solved by operator split in each spatial orientation, which can be given by semi-discrete forms at the n -th time step as follows:

$$\begin{aligned} \frac{\varphi^{(1)} - \varphi^n}{\Delta t} &= -\frac{1}{\Delta t} \frac{\partial F^n}{\partial x} + \varphi^n \frac{\partial u}{\partial x} \\ \frac{\varphi^{(2)} - \varphi^{(1)}}{\Delta t} &= -\frac{1}{\Delta t} \frac{\partial F^{(1)}}{\partial y} + \varphi^n \frac{\partial v}{\partial y} \\ \frac{\varphi^{n+1} - \varphi^{(2)}}{\Delta t} &= -\frac{1}{\Delta t} \frac{\partial F^{(2)}}{\partial z} + \varphi^n \frac{\partial w}{\partial z} \end{aligned} \quad (10)$$

Herein F with different superscripts is the flux calculated from the VOF interface reconstruction at each split step. More details of the algorithm can be found in (Yokoi, 2007). This method conserves the volume to high accuracy provided that (a) the time step is sufficiently small (typically a CFL number < 0.5 is necessary for the operator split) and (b) the velocity field is discretely divergence free (this may not be satisfied if IB geometries exist, see Section 5.3).

In this 2D example, an interface with surface normal vector (n_x, n_y) is approximated by the sum of two simple line reconstructions ϕ_x (dashed line) and ϕ_y (dot-segment line) with different weights

$$w_x = |n_x|/(|n_x| + |n_y|), \quad w_y = |n_y|/(|n_x| + |n_y|).$$

5. Numerical method

5.1. The Navier-Stokes solver

In this section, we first describe the basic implementation of the Navier-Stokes solver while ignoring the IB forcing term in the momentum equation. At the beginning of time step n , all VOF related quantities at the new step ($n+1$), i.e. ϕ^{n+1}, ρ^{n+1} and μ^{n+1} , are assumed to be known and they are referred with the superscript ($n+1$) dropped.

Our discretization approximates the Navier-Stokes equation and satisfies the incompressible condition by using a classical first-order projection method. In this method, the convective, viscous, gravity and surface tension terms are calculated explicitly. Next, a pressure Poisson equation is solved to obtain the pressure implicitly. Then the intermediate velocity is corrected to be discretely divergence free. The fractional-step algorithm is done by the following procedures.

A. Explicit Euler solve for predicting velocities:

$$\frac{\mathbf{u}^* - \mathbf{u}^n}{\Delta t} = -\nabla \cdot (\mathbf{u}\mathbf{u})^n + \frac{\mu}{\rho} \nabla^2 \mathbf{u}^n - \frac{1}{\rho} \sigma \kappa \delta \mathbf{n} + \mathbf{g} \quad (11)$$

B. Implicit pressure Poisson equation with variable coefficients:

$$\nabla \cdot \left(\frac{1}{\rho} \nabla p^{n+1} \right) = \frac{\nabla \cdot \mathbf{u}^*}{\Delta t} \quad (12)$$

C. Pressure projection step for correcting velocities:

$$\frac{\mathbf{u}^{**} - \mathbf{u}^*}{\Delta t} = -\frac{1}{\rho} \nabla p^{n+1} \quad (13)$$

The resulting velocity \mathbf{u}^{**} will be further modified according to the IB treatment, see Section 5.2.

The fluid domain is discretized on a standard uniform staggered grid. The components of velocity \mathbf{u} are arranged at the corresponding staggered positions (face-centered), while other flow fields are all defined at fluid cell centers (cell-centered). If field values are required at positions where they are not defined, linear interpolation of the neighboring points will be used. Similarly, spatial derivatives are computed by well-known second-order central difference scheme, except for the convective term. The following sections provide the spatial discretization schemes used in this study.

5.1.1. Convective term

For the non-linear convective term, a conservative discretization is used. For the u -component at staggered position $(i+1/2, j, k)$, it is given by

$$\nabla(\mathbf{u}\mathbf{u})_{i+1/2,j,k} = \nabla_x(uu) + \nabla_y(vu) + \nabla_z(wu).$$

Let us take the second term with y -derivative for an example. It is written in finite-difference form as

$$\nabla_y(vu) = \frac{v_{i+1/2,j+1/2,k} U_{i+1/2,j+1/2,k} - v_{i+1/2,j-1/2,k} U_{i+1/2,j-1/2,k}}{\Delta y},$$

where v is the advection velocity obtained using linear interpolation. The quantities U in capital letters are u -velocities constructed at the faces of momentum control volume. In general, upwind-biased schemes should be used to avoid unphysical oscillations. A hybrid scheme of (Spalding, 1972) with some modification is used to interpolate face values in this study. For the case of U velocity above, it can be determined by using the hybrid scheme as

$$U_{i+1/2,j+1/2,k} = \begin{cases} u_{i+1/2,j,k} & \text{if } Pe > Pe^{stab} \\ u_{i+1/2,j+1,k} & \text{if } Pe < -Pe^{stab} \\ (u_{i+1/2,j,k} + u_{i+1/2,j+1,k})/2 & \text{otherwise} \end{cases} \quad (14)$$

where the Peclet number (or cell Reynolds number), Pe , is chosen as the maximum value of two neighbor cells,

$$Pe = v_{i+1/2,j+1/2,k} \Delta y \max \left(\frac{\rho_{i+1/2,j,k}}{\mu_{i+1/2,j,k}}, \frac{\rho_{i+1/2,j+1,k}}{\mu_{i+1/2,j+1,k}} \right) \quad (15)$$

And Pe^{stab} is the stability criterion for which we use $Pe^{stab} = 1.5$ in this study. The terms in other directions are treated in a similar way. The hybrid scheme switches between first-order upwind difference scheme and second-order central difference scheme, depending on the local Peclet number. It is found to be a good company for the VOF method with large density ratios to avoid spurious wiggles at the free surface.

5.1.2. Surface tension

The famous continuum surface force (CSF) model (Brackbill et al., 1992) is used to compute the surface tension. In the CSF model, the surface force is recast as a volume force within a narrow band across the free surface as follows:

$$-\frac{1}{\rho} \sigma \kappa \delta \mathbf{n} \approx -\frac{1}{\rho} \sigma \kappa \nabla \varphi \quad (16)$$

In this study, the gradient term $\nabla \varphi$ is calculated on staggered grid points using central difference to keep the consistency with pressure calculation, as suggested by the balanced-force model of (Francois et al., 2006). The curvature κ is calculated from the divergence of the surface unit normal vector:

$$\kappa = \nabla \cdot \mathbf{n} \quad (17)$$

The interface unit normal vector \mathbf{n} is computed by evaluating the finite-difference gradient of the VOF function

$$\mathbf{n} = \nabla \varphi^s / |\nabla \varphi^s| \quad (18)$$

Here ϕ^s is a smoothed color function to replace the original ϕ field, which is a common technique to improve the estimation of normal vectors and curvatures in the VOF method, see e.g. (Gueyffier et al., 1999). In this study, ϕ^s is obtained by smoothing ϕ using the compact $3 \times 3 \times 3$ filter suggested by (Yabe et al., 2007). The smoothing operation is iterated twice to ensure that ϕ^s will span the interface within a band of several cells. It must be emphasized that, ϕ^s is used for normal vector exclusively, while other calculations including the gradient term $\nabla\phi$ in surface tension is based on the original ϕ .

In practice, we check the value of the VOF function and cutoff small, unstable values of normal vectors to ensure that the surface tension force is only calculated in the vicinity of the free surface. We note that, the present computational model of surface tension force is a reasonable choice for moderate and high Weber number flows, such as the violent free surface flows considered in this paper. On the other hand, for flows dominated by strong capillary effects such as bubbles and droplets, it is desirable that improved computational models should be used. For other models of surface tension force and their comparisons in the VOF framework, see (Baltussen et al., 2014).

5.1.3. Pressure projection

The left hand side of the pressure Poisson Eq. (12) is discretized by using a classical central difference scheme given by

$$\nabla \cdot \left(\frac{1}{\rho} \nabla p \right)_{ijk} = \frac{1}{(\Delta x)^2} \left(\frac{p_{i+1,j,k} - p_{ijk}}{\rho_{i+1/2,j,k}} - \frac{p_{ijk} - p_{i-1,j,k}}{\rho_{i-1/2,j,k}} \right) + \frac{1}{(\Delta y)^2} \left(\frac{p_{i,j+1,k} - p_{ijk}}{\rho_{i,j+1/2,k}} - \frac{p_{ijk} - p_{i,j-1,k}}{\rho_{i,j-1/2,k}} \right) + \frac{1}{(\Delta z)^2} \left(\frac{p_{i,j,k+1} - p_{ijk}}{\rho_{i,j,k+1/2}} - \frac{p_{ijk} - p_{i,j,k-1}}{\rho_{i,j,k-1/2}} \right) \quad (19)$$

The matrix system defined by this discrete operator is thus symmetric. The velocity divergence term at right hand side of the pressure Poisson equation can be easily calculated as

$$(\nabla \cdot \mathbf{u})_{ijk} = \frac{u_{i+1/2,j,k} - u_{i-1/2,j,k}}{\Delta x} + \frac{v_{i,j+1/2,k} - v_{i,j-1/2,k}}{\Delta y} + \frac{w_{i,j,k+1/2} - w_{i,j,k-1/2}}{\Delta z} \quad (20)$$

Once the pressure is obtained, the fluid velocity (e.g. the u -velocity) could be corrected by

$$\frac{u_{i+1/2,j,k}^{**} - u_{i+1/2,j,k}^*}{\Delta t} = - \frac{1}{\rho_{i+1/2,j,k}} \frac{p_{i+1,j,k} - p_{ijk}}{\Delta x} \quad (21)$$

To solve the discretized pressure equation, we use a multigrid-preconditioned conjugate gradient method from the HYPRE library² (namely the PFMG-CG structured grid solver). This solver is found to be efficient and robust through our numerical study even for gas–liquid flows with high density ratios (up to 1000:1). The convergence tolerance is set to 10^{-8} as a measure of the relative error.

5.2. IB treatment for flow conditions

The flow velocity at the wall is made consistent with the prescribed boundary velocity through the IB model. As mentioned in Section 3, each boundary wall has its own level set representation ψ_{Bm} ($m=1, 2, \dots, N$ for N objects). And for the entire fluid domain, both a level set function ψ_{ijk} and a solid volume fraction α_{ijk} field will be generated from the boundary shape profile.

Next the boundary velocity is to be projected from the Lagrangian wall objects to the Eulerian fluid mesh. The rigid velocity, \mathbf{u}_{Bm} , could be evaluated at a point \mathbf{x} using as follows:

$$\mathbf{u}_{Bm}(\mathbf{x}) = \mathbf{v}_{Bm} + \boldsymbol{\omega}_{Bm} \times (\mathbf{x} - \mathbf{x}_{Bm}) \quad (22)$$

where \mathbf{v}_B , $\boldsymbol{\omega}_B$ and \mathbf{x}_B are the linear velocity, angular velocity and reference point of rotation of the m th wall, respectively. We note that the point \mathbf{x} corresponds to a staggered velocity at cell face, so the components of \mathbf{u}_B parallel to the cell face are actually discarded. The calculation of \mathbf{u}_B is not only limited to the solid region inside the walls, but also expanded to a narrow band beyond the solid surface where the solid volume fraction α is non-zero. For a momentum control volume intersected by multiple wall objects, special care should be taken. We first find out whether the fluid point is covered by any of these objects by checking the signs of the level set functions. If so, the rigid velocity of that wall is directly assigned to the fluid position; otherwise a weighted mean boundary velocity is calculated with the volume fraction of each wall used as the weight.

Then the velocity \mathbf{u}^{**} from the fluid solver (Section 5.1) could be readily corrected to take into account the solid motion by an explicit modification:

$$\mathbf{u}^{n+1} = (1 - \alpha) \mathbf{u}^{**} + \alpha \mathbf{u}_B \quad (23)$$

which in return yields an expression for the IB forcing term

$$\mathbf{f}_B = \frac{\alpha(\mathbf{u}_B - \mathbf{u}^{**})}{\Delta t} \quad (24)$$

Explicit evaluation of \mathbf{f}_B is not necessary as only prescribed object motion is allowed. For a cell completely enclosed inside some solid subdomain ($\alpha=1$), the present IB correction (23) will directly inject the rigid velocity therein. Near the solid surface ($0 < \alpha < 1$), the velocities are continuously interpolated forming a boundary layer by which fluid and solid regions are smoothly connected. The forcing effect naturally vanishes in the fluid region ($\alpha=0$).

Applying Eq. (23) to a staggered velocity variable still requires some more clarification. This is illustrated in Fig. 2 where the yellow region corresponds to the IB domain. Based on SDF at cell centers, the fluid cells can be categorized as fluid points ($\psi > 0$) and solid points ($\psi \leq 0$). The face velocity that needs the velocity correction is called an IB point, which is identified by that the wall level set function ψ is non-positive for at least one of the two adjacent cells. We take the u -velocity ($i+1/2, j, k$) as an example. It is treated as an IB point if the values of ψ at adjoining cells sharing

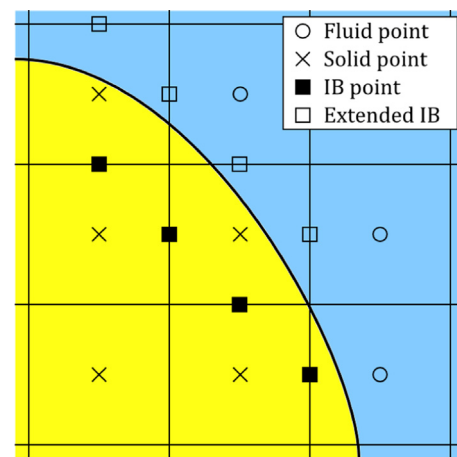


Fig. 2. Selecting IB points on a staggered grid. (For interpretation of the references to color in this figure, the reader is referred to the web version of this article).

² The HYPRE library, <http://acts.nersc.gov/hypre/>.

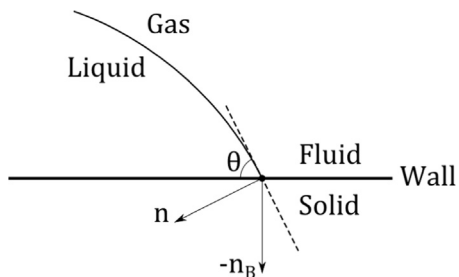


Fig. 3. Schematic diagram of contact angle at a wall.

this face satisfy the relation

$$(\psi_{ijk} < 0 \text{ and } \psi_{i+1,j,k} < 0) \text{ or } \psi_{ijk} \cdot \psi_{i+1,j,k} \leq 0. \quad (25)$$

This criteria is able to help identify IB points completely covered by the IB domain as well as those extending to the first layer of fluid positions that are possibly affected by the immersed boundary, as shown in Fig. 2.

Another problem is how to setup the boundary condition (BC) when the immersed boundary extends to the physical boundary, as that for internal flows. Based on our numerical test, at the domain boundary taken over by IB regions, one can simply apply consistent fluid BCs, e.g. Dirichlet BC for velocity and homogeneous Neumann BC for pressure.

5.3. IB treatment for fluid interface

A typical IB method for fluid-solid problems takes care of the no-slip velocity BC, but an additional consideration arises when free surface calculation is involved. Usually a special boundary condition has to be supplied to the intersection of the free surface and the solid wall, viz. the contact angle BC, which is given as follows with a contact angle θ :

$$\mathbf{n} \cdot (-\mathbf{n}_B) = \cos(\theta) \quad (26)$$

in which \mathbf{n} is the interface unit normal pointing from gas region to liquid region and \mathbf{n}_B is the boundary unit normal pointing from solid region to fluid region, as defined in preceding sections. Their relations is illustrated for a two-dimensional contact point in Fig. 3.

Because the precise resolution of contact line dynamics is not the main aim, our discussion is restricted to the basic case of a neutral contact angle, i.e. $\theta=\pi/2$, although the extension to other conditions is likely to be made. Consequently, the contact angle BC (26) is reduced to

$$\mathbf{n} \cdot (-\mathbf{n}_B) = -\frac{\nabla \varphi}{|\nabla \varphi|} \cdot \mathbf{n}_B = \cos\left(\frac{\pi}{2}\right) \text{ or } \nabla_B \varphi = 0 \quad (27)$$

This reduced BC (27) equals to a homogeneous Neumann BC for the VOF function at solid walls. In this study, two different approaches based on the extrapolation of the VOF function into the solid region are used to satisfy the contact angle BC.

The first way is a simple ‘dilation’ operation which has been inspired by some sharp-interface methods that smoothly populate pressure (Choi et al., 2007) or velocity (Arienti and Sussman, 2014) into the solid domain. In the beginning, all fluid cells ($\psi > 0$) are tagged and all solid cells ($\psi \leq 0$) are untagged. Next the VOF function inside an untagged cell will be assigned as the average value from tagged cells in its $3 \times 3 \times 3$ neighborhood with weight factors inversely proportional to the square of the distance between them. This procedure is repeated for n^{extend} times. Every time a cell is updated, it will be tagged and treated as known in the next iteration. In this way, the VOF front in the fluid region will be marched into the solid region sequentially, by one layer of cells per iteration.

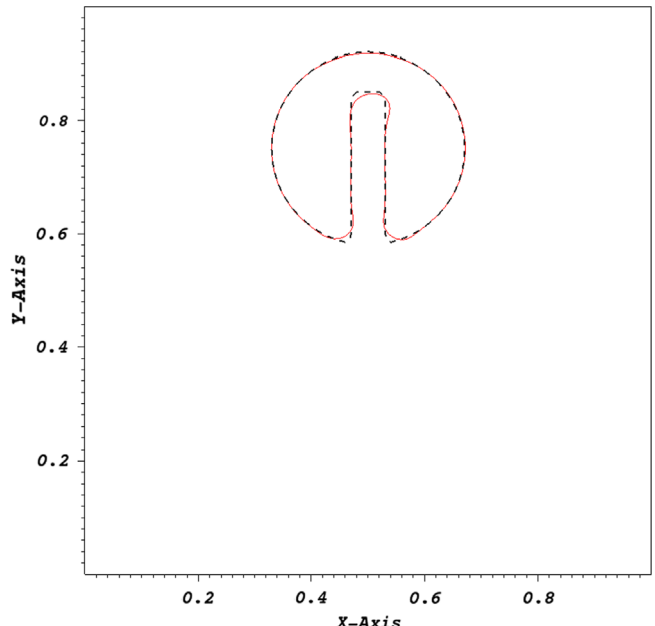


Fig. 4. Zalesak disk problem using THINC/WLIC scheme. (For interpretation of the references to color in this figure, the reader is referred to the web version of this article).

The second way consists in iteratively solving the ‘extension’ equation of (Sussman, 2001):

$$\frac{\partial \varphi}{\partial \tau} + \mathbf{u}^{\text{extend}} \cdot \nabla \varphi = 0 \quad (28)$$

The extension velocity is the normal vector orthogonal to the solid surface:

$$\mathbf{u}^{\text{extend}} = -\mathbf{n}_B \quad (29)$$

Although originally Eq. (28) is proposed for the LS method, we apply it to VOF functions. It is solved at all the solid cells ($\psi \leq 0$) for an artificial time duration $\tau^{\max} = n^{\text{extend}} \Delta x$ with time increment $\Delta \tau = \Delta x$. A semi-Lagrangian advection scheme is used to find φ from its upwind position:

$$\varphi_{ijk}^{\tau+\Delta\tau} = \varphi^{\tau}(\mathbf{x}_{ijk} - \mathbf{u}^{\text{extend}} \Delta \tau) \quad (30)$$

for which the right hand side is evaluated by using a trilinear interpolation. It is also possible to implement general contact angle BC in the current IB framework by using the extension method. This can be readily achieved by determining the extension velocity $\mathbf{u}^{\text{extend}}$ based on the local solid surface normal vector, interface orientation and contact angle, while other parts of the numerical procedure remain unchanged. See (Sussman, 2001) and (Yokoi, 2013) for the derivation of $\mathbf{u}^{\text{extend}}$ with general contact angles.

The dilation approach has the advantage in its simplicity that only the sign of the solid level set function is required, which makes it efficient and applicable to complicated geometry configurations. However, it must come with considerable smearing of the extrapolated interface. The extension approach reflects the solid surface orientation and thus can be adopted for arbitrary contact angles, but finding the surface normal vector is sometimes ambiguous for unresolved areas (e.g. consider a single cell influenced by two objects). Both methods can take the advantage of satisfying the contact angle BC without explicitly locating the three-phase contact line. They are also shown to give similar results through our numerical tests. The parameter n^{extend} is the total iteration number that controls the depth of front advancing into the solid region. Setting n^{extend} to zero is equivalent to

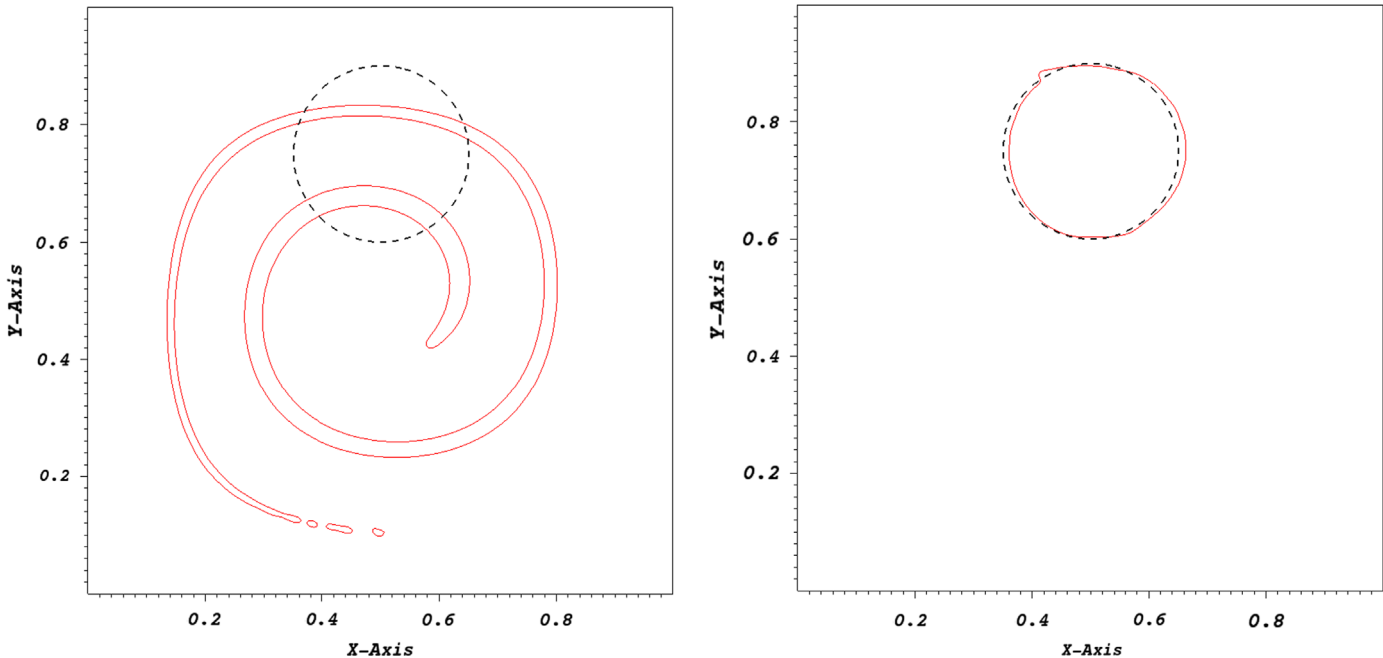


Fig. 5. Rider-Kothe vortex problem using THINC/WLIC scheme: interface at $t=T/2$ (left) and $t=T$ (right). (For interpretation of the references to color in this figure, the reader is referred to the web version of this article).

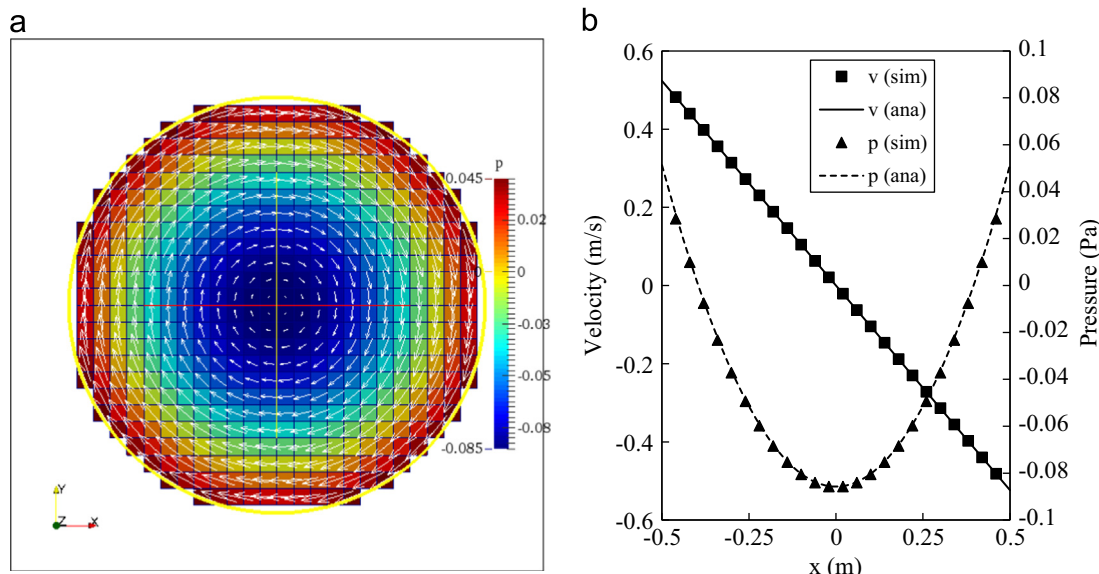


Fig. 6. Flow in rotating circular boundary: (a) pressure contour and velocity vectors and (b) plot of pressure and velocity on x -axis.

omitting the contact angle BC. If not specified, we have $n^{\text{extend}}=4$ in this study for both approaches.

It is noted that, in the present method, the interface advection is performed for all computational cells including immersed boundaries. And then the dilation or extension procedure is carried out to modify the VOF function in partial and full solid cells. This treatment is consistent with the IB methodology. However, the VOF advection is no longer conservative in the existence of the immersed boundary. A slight mass error might occur as the velocity field modified by IB forcing does not satisfy the discrete divergence free condition near the solid boundary, which may further accumulate with time evolution. If the rigorous conservation of fluid volume is desired, we choose to periodically reset the volume fractions of the liquid phase to compensate the mass error, which does not have an appreciable influence to the overall flow behavior. It is done by calculating the global volume

error and simply subtracting the mean error from the VOF function in interface cells indicated by $0 < \phi < 1$ and $\psi > 0$. This procedure to achieve global conservation shifts the interface position towards the desired phase volume. It is similar to that used in the front-tracking method (Bunner and Tryggvason, 2002) or the level set method (Fujita et al., 2015), and it is more simple and straightforward in the VOF framework.

5.4. Time-stepping algorithm

In the present method, the time step Δt is limited by the CFL condition, viscosity and surface tension:

$$\Delta t < C \cdot \min\left(\frac{\Delta x}{|\mathbf{u}|_{\max}}, \frac{\rho \Delta x^2}{\mu}, \sqrt{\frac{\rho \Delta x^3}{2\pi\sigma}}\right) \quad (36)$$

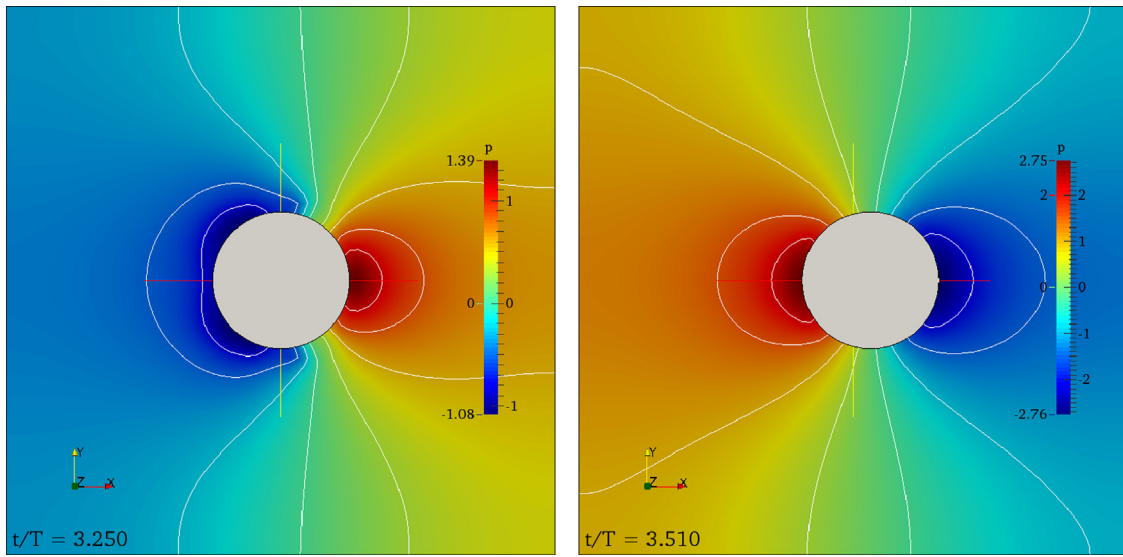


Fig. 7. Pressure contours around the oscillating cylinder.

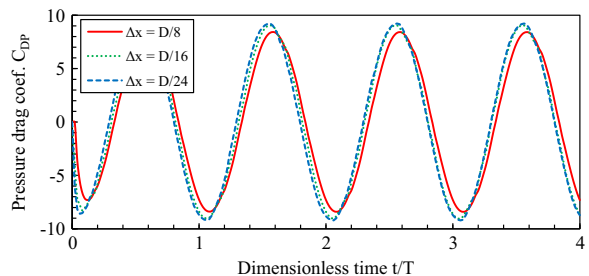


Fig. 8. Pressure drag coefficient of the oscillating cylinder with mesh refinements.

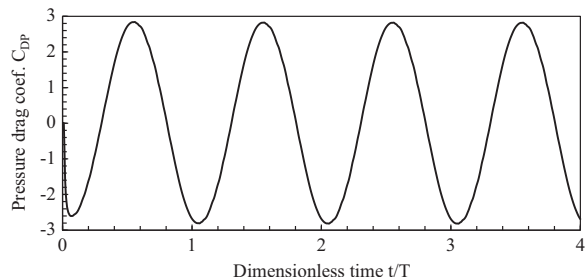


Fig. 10. Pressure drag coefficient of the oscillating sphere.

with C a positive constant that is sufficiently small. We perform simulations with a stable fixed time step chosen accordingly. We note that, the current explicit treatment of viscous and surface tension terms may cause stringent limitations of time step for high viscosity or strong capillary effects on fine meshes (although this is not a problem for the present study as they are not dominant). In that case, one may use semi-implicit predictor-corrector algorithms to remove those constraints, see e.g. (Sussman and Ohta, 2009).

The overall time-stepping algorithm in a single sweep (from step n to $n+1$) is outlined as follows.

Step 1. Update moving boundaries for the arbitrary-shape wall boundary model, see Section 3.

Step 2. Transfer the boundary representation to the fluid grid, on which generate the solid wall level set ψ^{n+1} and volume fraction α^{n+1} , see Section 3.

Step 3. Advance the VOF interface to ϕ^{n+1} using the THINC/WLIC scheme, see Section 4.

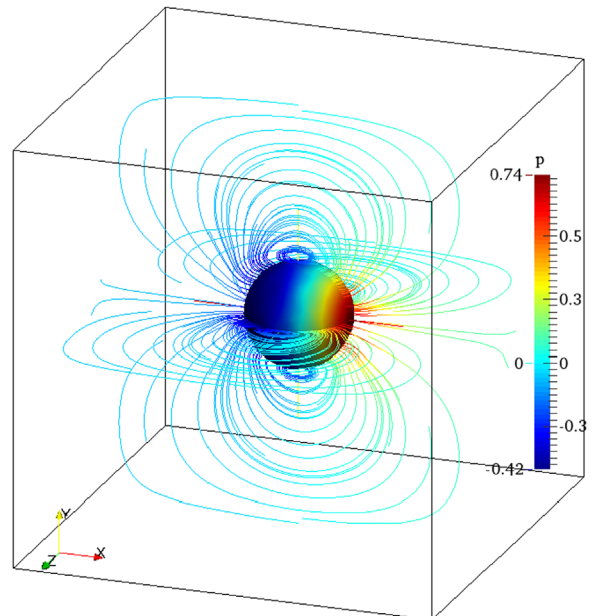


Fig. 9. Streamlines and pressure contours around the oscillating sphere.

Step 4. Extend the VOF function into the solid region, by using either the dilation or extension operation described in Section 5.3.

Step 5. Compute the updated fluid properties ρ^{n+1} and μ^{n+1} .

Step 6. Explicitly calculate the convective, viscous, gravity and surface tension terms listed in Section 5.1 to obtain a provisional velocity \mathbf{u}^* .

Step 7. Solve the pressure Poisson equation for p^{n+1} , and correct the intermediate velocity to have \mathbf{u}^{**} , see Section 5.1.3.

Step 8. Apply the IB treatment to enforce the velocity BC at the walls, and finally the flow velocity is updated as \mathbf{u}^{n+1} , see Section 5.2.

6. Numerical validations

In this section, we test our implementation of the VOF method and the IB method separately. Those numerical tests are

performed in pseudo-2D systems and computed results are compared with analytical solutions.

6.1. VOF advection

In order to validate the THINC/WLIC VOF interface calculation, two scalar advection problems with prescribed velocity fields are calculated. We first consider the famous Zalesak disk problem (Zalesak, 1979) with rigid body rotation. In this test, the computational domain is set to a unit square and a notched disk whose radius is 0.17 is centered at (0.5, 0.75). The slit cutting into the disk is given by the area of $|x - 0.5| \leq 0.03$ and $y \leq 0.85$. The VOF function inside the disk is initialized to one. A velocity field is prescribed as $u = y - 0.5$ and $v = 0.5 - x$. After the simulation begins, the disk will rotate rigidly clockwise around the domain center. We run the computation on a 100 by 100 grid and complete one revolution in 2000 steps. Fig. 4 shows the computational results after one cycle of rotation. The original shape of the notched disk is clearly recovered by the results, except for some smearing and

deformation at sharp corners, which could be improved by further refining the grids. It is seen that the adopted VOF scheme can well predict the interface motion.

The red line shows the interface after one rotation and the black dashed line is the initial shape.

Another problem, referred to as the Rider-Kothe vortex (Rider and Kothe, 1998), is a more severe test featured by a large deformation of the interface. At $t=0$, a circle with radius 0.15 is placed at (0.5, 0.75). A time dependent shearing flow is imposed as

$$u(t) = -U_0 \sin^2(\pi x) \sin(2\pi y) \cos(\pi t/T)$$

$$v(t) = U_0 \sin^2(\pi y) \sin(2\pi x) \cos(\pi t/T)$$

in which T is the time period for the circle returning back to its initial position. In this test, we have $U_0=1$ and $T=8$. The (u, v) values are directly assigned to staggered velocity components at cell faces. We use a 200 by 200 uniform grid to discretize the computational domain of 1.0 by 1.0. A fixed time step of 0.001 s is

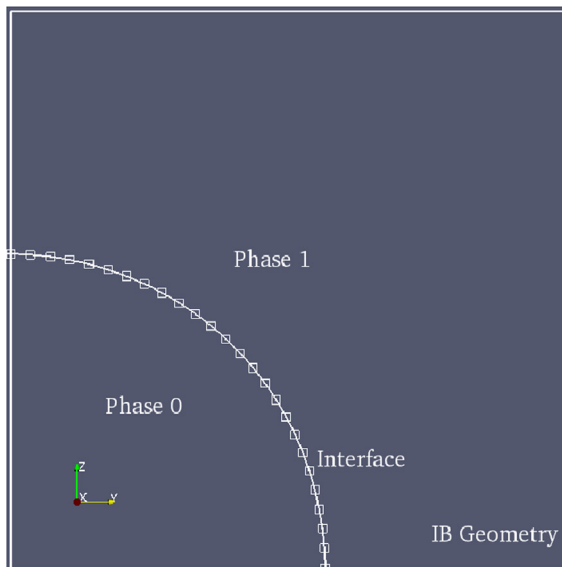


Fig. 11. Relaxed drop shape (left) and pressure (right) in rectangular IB geometry.

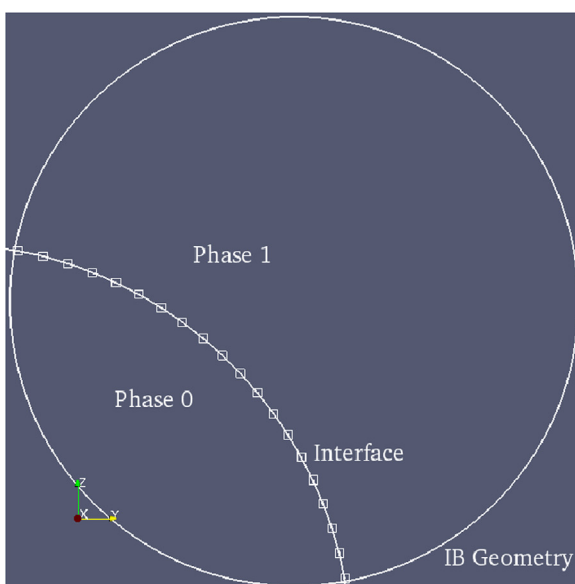
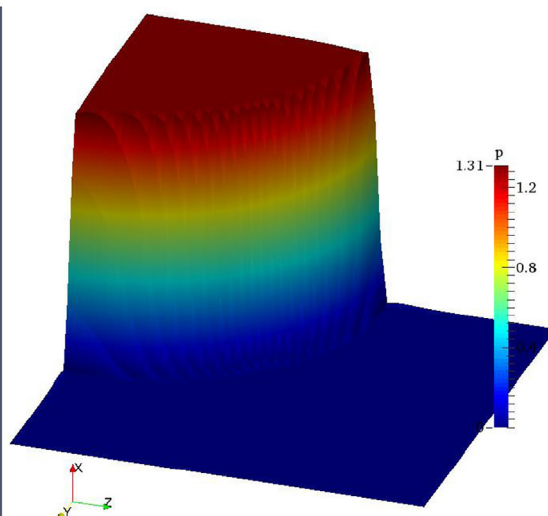
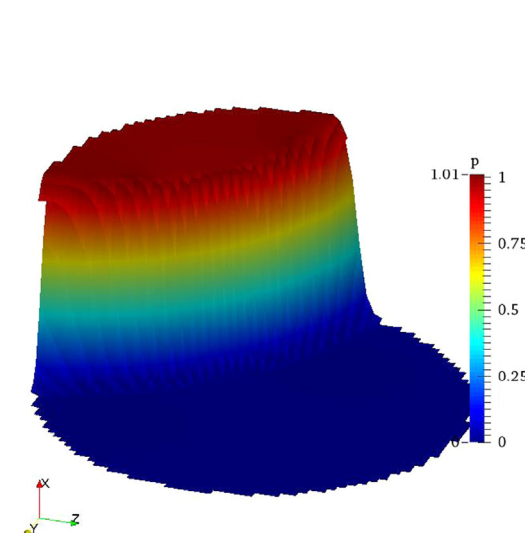


Fig. 12. Relaxed drop shape (left) and pressure (right) in circular IB geometry.



chosen to guarantee a mediate Courant number. After 8000 steps the simulation is finished.

Fig. 5(a) shows the interface shape with maximal deformation at $t=T/2$. The original circle has been stretched into a long filament along the vortex flow direction, whereas some flotsam detached from the filament tail which has becomes too thin to be resolved by the current grid. When time comes to $t=T$, the circular shape should be restored. **Fig. 5(b)** compares the simulation results with the initial state. Although there is small difference between the calculated interface and the initial state, the overall agreement between them is satisfactory. This shows that the current VOF model can be readily applied to flows with large interface deformations.

The red line shows the calculated interface and the black dashed line is the original shape.

6.2. Static IB geometry

Next, in order to show that the IB model is able to simulate the interaction between the fluid and the boundary in motion, the flow driven by a rotating circular boundary is computed. The simulation is performed within a pseudo-2D rectangular domain

accommodating a cylindrical SDF object whose diameter is $D=1.0\text{ m}$ and its angular velocity is $\omega=\pi/3$. The fluid density is $\rho=1.0\text{ kg/m}^3$ and the dynamic viscosity is $\mu=0.1\text{ Pa s}$. Hence the Reynolds number based on the rotation speed, diameter and fluid kinematic viscosity is sufficiently low ($\text{Re}<10$) to converge to a steady state. The grid spacing is $\Delta x=D/25$ and the time step is $\Delta t=0.5\text{ ms}$.

Fig. 6(a) illustrates the pressure contour and velocity vectors obtained after the flow reaches a steady state. We note that, since the data in immersed boundary domain is irrelevant to the analysis, only true fluid cells indicated by $\psi>0$ are shown in this image. It is clearly observed that the flow is rotating around the center of the circle and a low-pressure region is found near the center owing to the centrifugal effect. The flow velocity and pressure on x -axis are plotted and compared with their analytical values in **Fig. 6(b)**. For the velocity, a linear distribution of $v=\omega r$ is obtained with r the distance from the center; for the pressure, a quadratic profile $p=0.5\rho\omega^2r^2+p_0$ is expected with p_0 an arbitrary constant. Numerical results for both velocity and pressure agree well with the analytical solutions.

6.3. Moving IB geometry

In addition to the previous test, the ability to treat moving IB geometry is examined in this section. The fluid drag force in static sphere arrays has been examined in our previous study (Sun and Sakai, 2015). In this study, as the modeling of solid boundaries with rigid motions is important, the fluid forces acting on moving immersed objects will be simulated.

The oscillating cylinder problem proposed by (Seo and Mittal, 2011) is computed first. In this test, a cylinder whose diameter is D moves on the horizontal x -axis subject to a harmonic oscillation with the amplitude A and frequency f . Its center position and velocity are given as follows.

$$x(t) = -A \cos(2\pi ft)$$

$$u(t) = U \sin(2\pi ft)$$

$$U = 2\pi f A$$

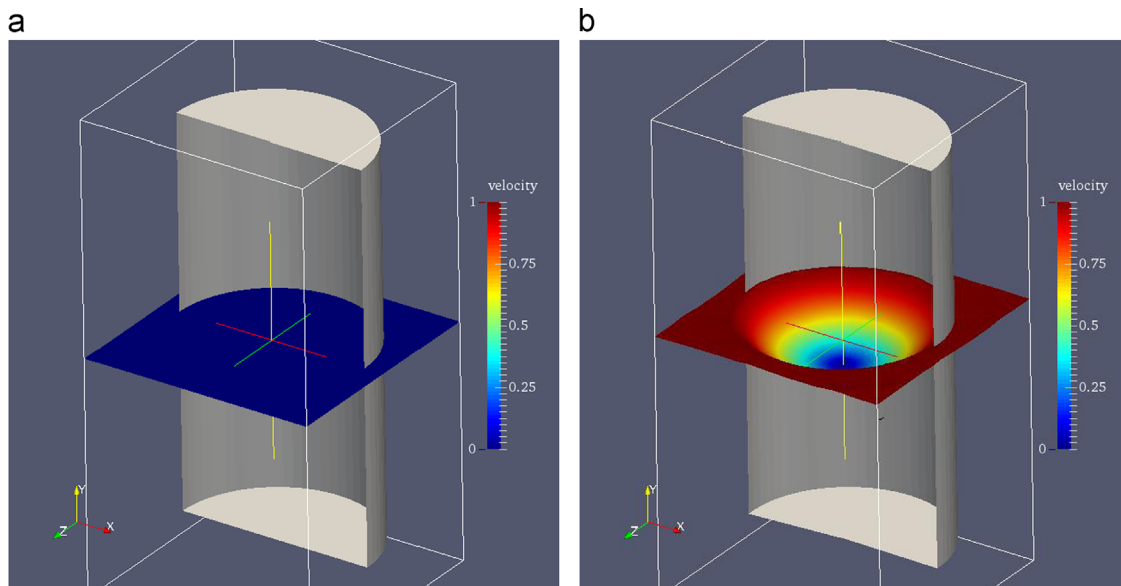


Fig. 13. The interface shape in a rotating barrel: (a) initial state and (b) steady state.

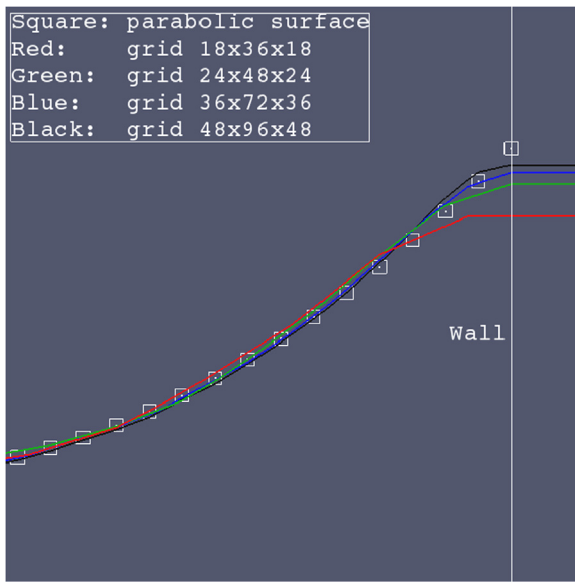


Fig. 14. Comparison of the interface shape with grid refinement.

Table 3
Computational conditions for the dam break problem.

Gravity (m/s^2)	9.8
Liquid density (kg/m^3)	1000
Liquid viscosity (Pa s)	10^{-3}
Gas density (kg/m^3)	1.0
Gas viscosity (Pa s)	10^{-5}
Time step (s)	10^{-4}
Grid size (m)	4.5625×10^{-3}

The instantaneous pressure drag coefficient C_{DP} is calculated by integrating the fluid pressure on the IB contours defined by $\psi=0$.

$$C_{DP} = \frac{\left| \int_B p \mathbf{n}_B dS \right|}{0.5 \rho D^3 f^2}$$

The diameter is $D=1.0$ m, and the quasi-2D computational domain is a box of $-2D \leq x, y \leq 2D$. We have the amplitude $A=D/8$ and the frequency $f=1.0$ Hz. The fluid density is $\rho=1.0 \text{ kg/m}^3$ and the kinematic viscosity is $\nu=0.01 \text{ m}^2/\text{s}$. Therefore, the characteristic velocity is $U=0.7854 \text{ m/s}$. As for non-dimensional parameters defining the flow, the Reynolds number is estimated to be $Re=UD/\nu=78.54$ and the Strouhal number is $St=fD/U=D/2\pi A=1.273$.

Simulations are carried out on fluid meshes with refined cell sizes of $\Delta x=D/8$, $D/16$ and $D/24$, respectively. The time step is also adjusted simultaneously to keep the CFL number equal to 0.1256. Fig. 7 displays the pressure contours around the oscillating cylinder at different time instants. In Fig. 8 the pressure drag coefficient C_{DP} is plotted as a function of time. From the comparison of different grid spacing, the results seem to be convergent. The maximum absolute value is $C_{DP}=9.27$, which is reasonably close to the result of (Seo and Mittal, 2011) (approximately $C_{DP}=10$ read from their Fig. 12).

Additionally, another oscillating sphere problem in (Seo and Mittal, 2011) is computed as a 3D test problem. The computational domain is a cube of $-2D \leq x, y, z \leq 2D$. The sphere has diameter of $D=1.0$ m and the cell size is set to $\Delta x=D/16$. Other computational conditions are the same as the previous cylinder test. Fig. 9 shows the streamlines around the oscillating sphere and the solid surface colored by fluid pressure. The temporal variation of C_{DP} is plotted in Fig. 10, from which the peak value is $C_{DP}=2.83$ that agrees with

(Seo and Mittal, 2011) (approximately $C_{DP}=3.0$ read from their Fig. 17).

In fact, (Seo and Mittal, 2011) has pointed out that IB methods can generate spurious fluctuations in the pressure field around moving objects, and they proposed a sharp-interface IB method based on the cut-cell technique to solve this problem. We confirmed this numerical artifact in the oscillating cylinder problem by using extensively refined space and time resolutions, which is similar to the report of (Arienti and Sussman, 2014). Although it is not fully free of spurious pressure oscillations, the estimation of fluid drag is in good agreement with that obtained in (Seo and Mittal, 2011) using a more complicated algorithm. In general, the performance of the IB model employed in this study is thought to be satisfactory to represent arbitrary-shaped walls and moving bodies in a simple and efficient way.

6.4. Surface tension

In this section we test the surface tension calculation together with the contact angle treatments by studying the relaxation of quasi-2D drops to static shape in different IB geometries.

We first design a test case with straight walls. The computational domain is defined on $-0.03 \leq x \leq 0.03$ and $-0.06 \leq y, z \leq 0.06$ with a discretization of $32 \times 64 \times 64$ cells. A box $-L/2 \leq x \leq L/2$ and $-L \leq y, z \leq L$ is embedded as the IB geometry. The reference length L equals 0.05 m. Under this problem setup, the immersed boundary does not coincide with any cell boundaries. We initialize the VOF function to $\phi=1$ in the third quadrant ($-L \leq y, z \leq 0$) and fill with $\phi=0$ elsewhere. The gravity is set to zero, and other parameters are chosen as $\rho_l=\rho_g=1.0 \text{ kg/m}^3$, $\mu_l=0.001 \text{ Pa s}$, $\mu_g=10^{-5} \text{ Pa s}$ and $\sigma=0.075 \text{ N/m}$. The dimensionless Laplace number is estimated to be $\text{La}=\sigma\rho(2L)/\mu^2=7500$.

Subject to the 90° contact angle condition, the initial square drop will relax to a quarter of a circle whose radius is $a=0.0564$ corresponding to a Laplace pressure $\sigma/a=1.330 \text{ Pa}$. In Fig. 11(a), we compare the computed interface shape (solid line) with the expected state (square symbols). It is seen that they are in good agreement. The pressure profile in the fluid domain is shown in Fig. 11(b), in which a sharp gradient across the drop interface is observed. The pressure jump is calculated to be $\Delta p=1.303 \text{ Pa}$, which is close to the predicted Laplace pressure.

Next we consider a system with curved boundaries. The parameters are the same as previous test except that the IB geometry is replaced by a cylinder with radius $R=L$. On a section plane, the static surface will theoretically be an arc of a circle with radius $a=0.0724$ and central angle of 69.3° . In Fig. 12(a), the interface (solid line) after relaxation is shown in comparison with the expected shape (square symbols). Fig. 12(b) plots the pressure in the circular fluid domain. The error in the pressure jump is still modest compared with the Laplace pressure, see Table 1.

As noted previously, it is possible to improve the surface tension calculation for low-We flows by introducing the sharp-interface modeling and height function-based curvature following (Francois et al., 2006). Compared with those techniques coming with considerable complications of algorithm, the present surface tension model, although less accurate, seems to work well in the scope of two-phase flows for this study. In addition, it also allows for a straightforward integration with the complex geometry modeling.

7. Numerical examples

In this section, we show three-dimensional numerical examples using the VOF-IB method. First, the present method is validated for the ability to calculate interface deformation caused by a rotating, circular geometry. This is done for a quasi-steady system,

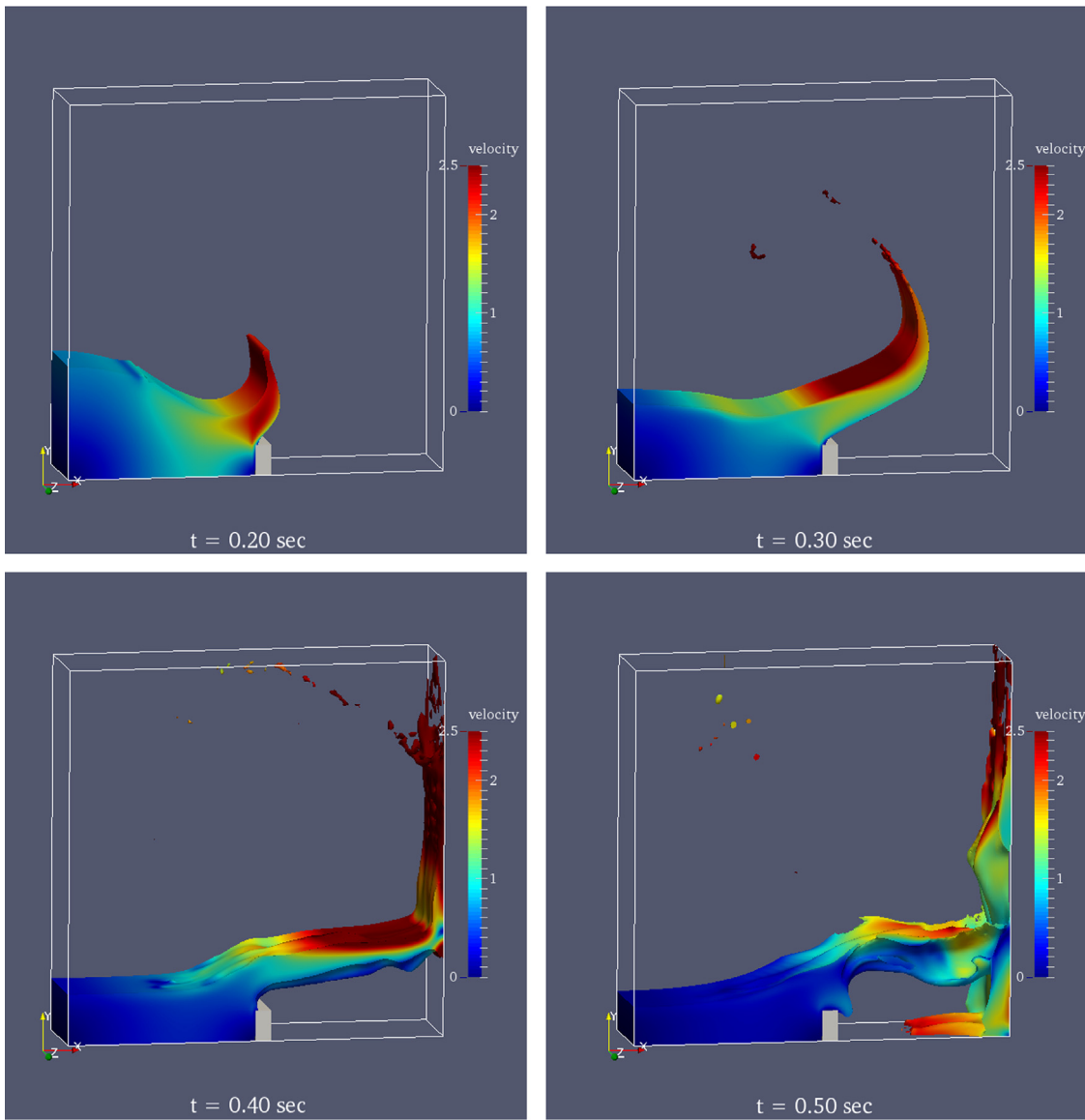


Fig. 15. 3D snapshots of the dam break flow hitting an obstacle with velocity contour.

namely the parabolic free surface in a rotating barrel. The second flow case features energetic interaction between the air–water flow and the solid boundary, as that happens for many industrial flows involving violent free surface motion. In this test, a dam break flow hitting an obstacle is simulated and validated against experimental data. Finally, as an illustration of the potential application of the VOF–IB method, we present numerical simulations of a laboratory two screw kneader with partially filled liquid inside.

7.1. Water surface in a rotating barrel

This test problem studies the two-phase flow motion in a rotating geometry by demonstrating the interface deformation subject to a steady revolving state, which is related to devices like centrifuges. In a rotating barrel, the steady state of a free surface under rigid body rotation, ignoring the contact condition at the rigid wall, is given by a parabolic profile:

$$z = \frac{\omega^2}{2g} r^2 + \left(H - \frac{\omega^2 R^2}{4g} \right)$$

where z is the surface elevation, r is the distance from rotation axis, ω is the angular velocity, g is gravity, H is the initial water depth, and R is the radius of the cylindrical container. We simulate a barrel with radius $R=1$ and height $2H$ rotating with $\omega=1$. The initial water depth H equals to 2 and the gravity is $g=-1$. The computational domain is set to $2.4 \times 4.8 \times 2.4$ and the barrel is placed at the center of the domain with its pole aligned with the y -axis. The density and dynamic viscosity is $\rho_l=1.0$ and $\mu_l=0.01$ for the liquid phase, and $\rho_g=0.001$ and $\mu_g=10^{-5}$ for the gas phase, respectively. For this hypothetical test problem, the Reynolds number based on rotation speed, barrel radius and liquid properties is $Re=\rho\omega R^2/\mu=100$, and the Froude number is $Fr=\omega R/(Rg)^{1/2}=1$. The computation is run up to steady state using different resolutions, $18 \times 36 \times 18$, $24 \times 48 \times 24$, $36 \times 72 \times 36$ and $48 \times 96 \times 48$ cells, which serves as a grid convergence study involving the fluid interface. See Table 2 for the simulation conditions.

Fig. 13 shows the initial and final shapes of the interface obtained using the finest grid ($48 \times 96 \times 48$ cells). Due to centrifugal effects, the liquid has been pushed towards the wall side. Thus a concave surface forms and it is elevated from the initial position near the wall. In addition, as a 90° contact angle BC is

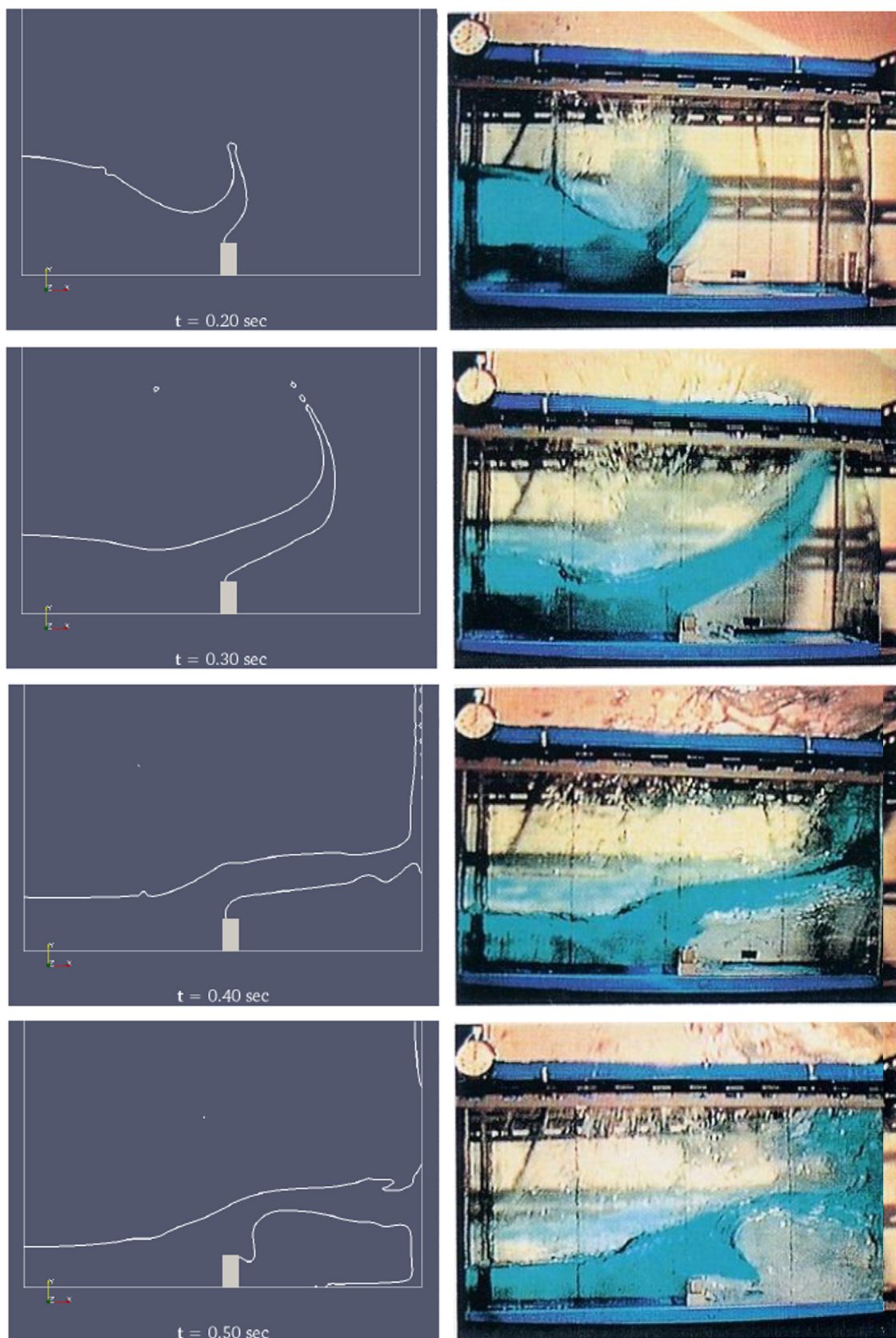


Fig. 16. Comparison between the calculated interface (left column) and experimental photographs (right column).

applied, we can see that a flat extension of the interface is generated in the solid region on a plane orthogonal to the vertical wall. In Fig. 14 the grid refinement study is shown in respect of the

interface shape. Convergent results are obtained as grid is refined, and the interface shapes are also in good agreements with the analytical solution. Some difference between the simulation

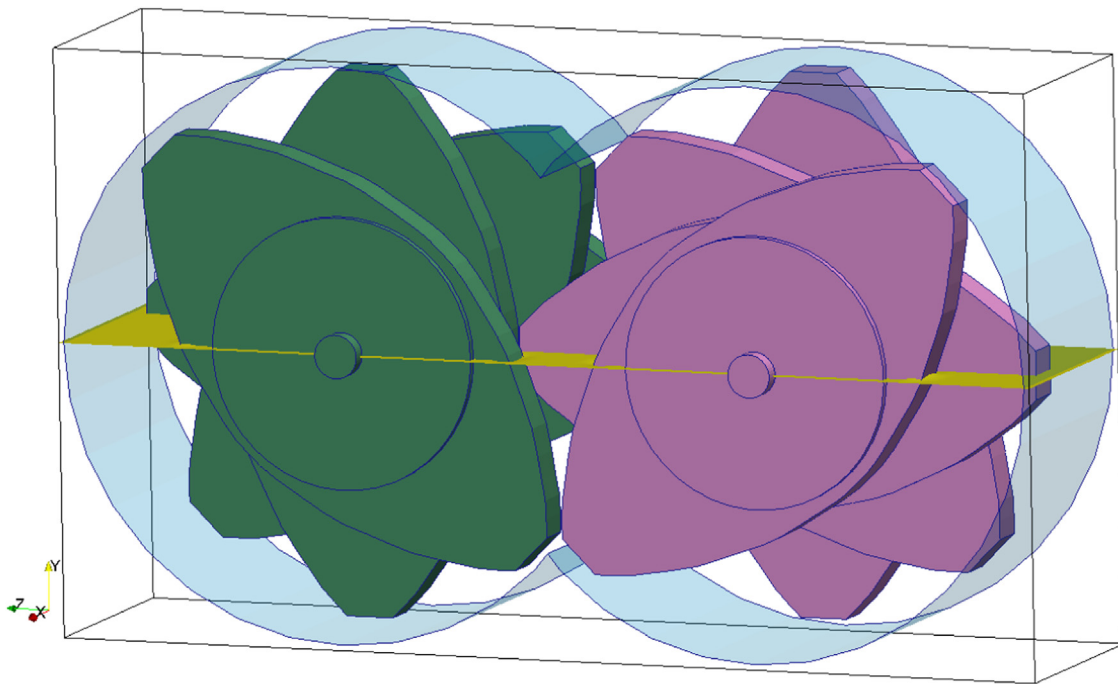


Fig. 17. Initial setup of the TSK problem. The yellow plane indicates the position of the initial water surface. (For interpretation of the references to color in this figure legend, the reader is referred to the web version of this article.)

Table 4
Computational conditions for the TSK simulation.

	Case 1	Case 2	Case 3
Liquid density (kg/m^3)	1000		
Liquid viscosity (Pa s)	10^{-3}		
Gas density (kg/m^3)	1.0		
Gas viscosity (Pa s)	10^{-5}		
Surface tension (N/m)	0.075		
Grid spacing (m)	2×10^{-3}		
Time step (s)	1×10^{-4}		
Rotation speed (rpm)	30	60	90

results and the parabolic profile is near the contact line at the wall. This is consistent with the application of the contact angle BC; however, this point is not considered in the analytical solution.

7.2. Dam break flow over an obstacle

The dam break problem is a classical free surface or two-phase flow test case with violent free surface motion and air entrainment. In this section, we simulate an intense dam break problem in which the collapsing water hits on an obstacle before impacting against the wall. This test problem is suggested by (Koshizuka et al., 1995) and studied therein numerically using a Lagrangian particle method with experimental backup. We follow the problem setup described in (Koshizuka et al., 1995) and add a solid obstacle at the bottom of the tank. The obstacle is modeled by the IB method. The water has density $\rho_l=1000 \text{ kg}/\text{m}^3$ and the air $\rho_g=1 \text{ kg}/\text{m}^3$, while their viscosities are $\mu_l=0.001 \text{ Pa s}$ and $\mu_g=10^{-5} \text{ Pa s}$. Non-slip boundary conditions are applied to all walls. With the initial length of the dam denoted by a , we compute the solution with a uniform grid spacing $\Delta x=a/32$ and a fixed time step $\Delta t=10^{-4} \text{ s}$, see Table 3.

The calculated 3D fluid interface is presented in Fig. 15 at time instants $t=0.2, 0.3, 0.4$ and 0.5 s . Sliced views of these results are compared in Fig. 16 with the experimental photographs of (Koshizuka et al., 1995). We can see that the flow behavior has

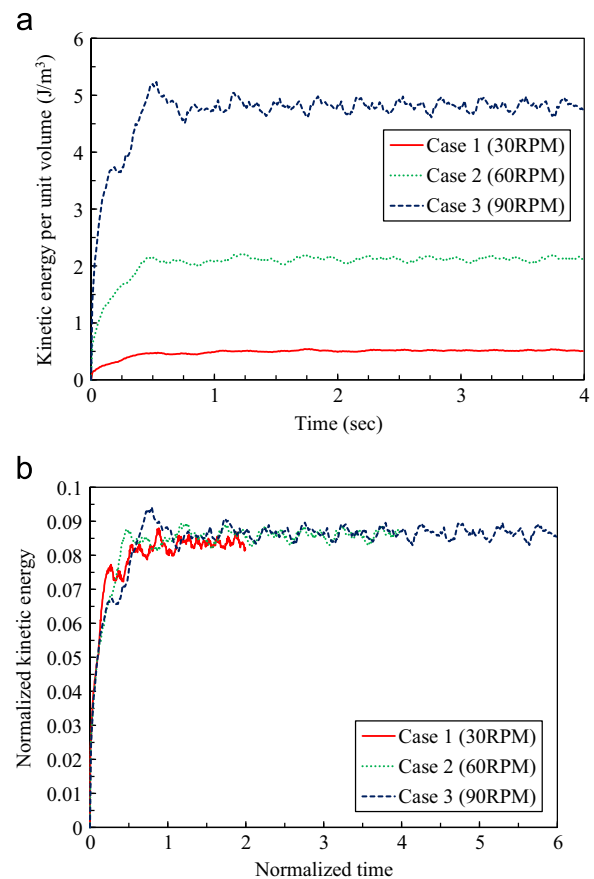


Fig. 18. Temporal variation of kinetic energy of two-phase flows in the TSK: (a) plot of kinetic energy against time and (b) plot of normalized kinetic energy against dimensionless time.

been drastically changed by the deflection at the obstacle. A strong, curved arm outspreads from the water body and flies towards the opposite wall ($t=0.2$ and 0.3 s). After the water arm

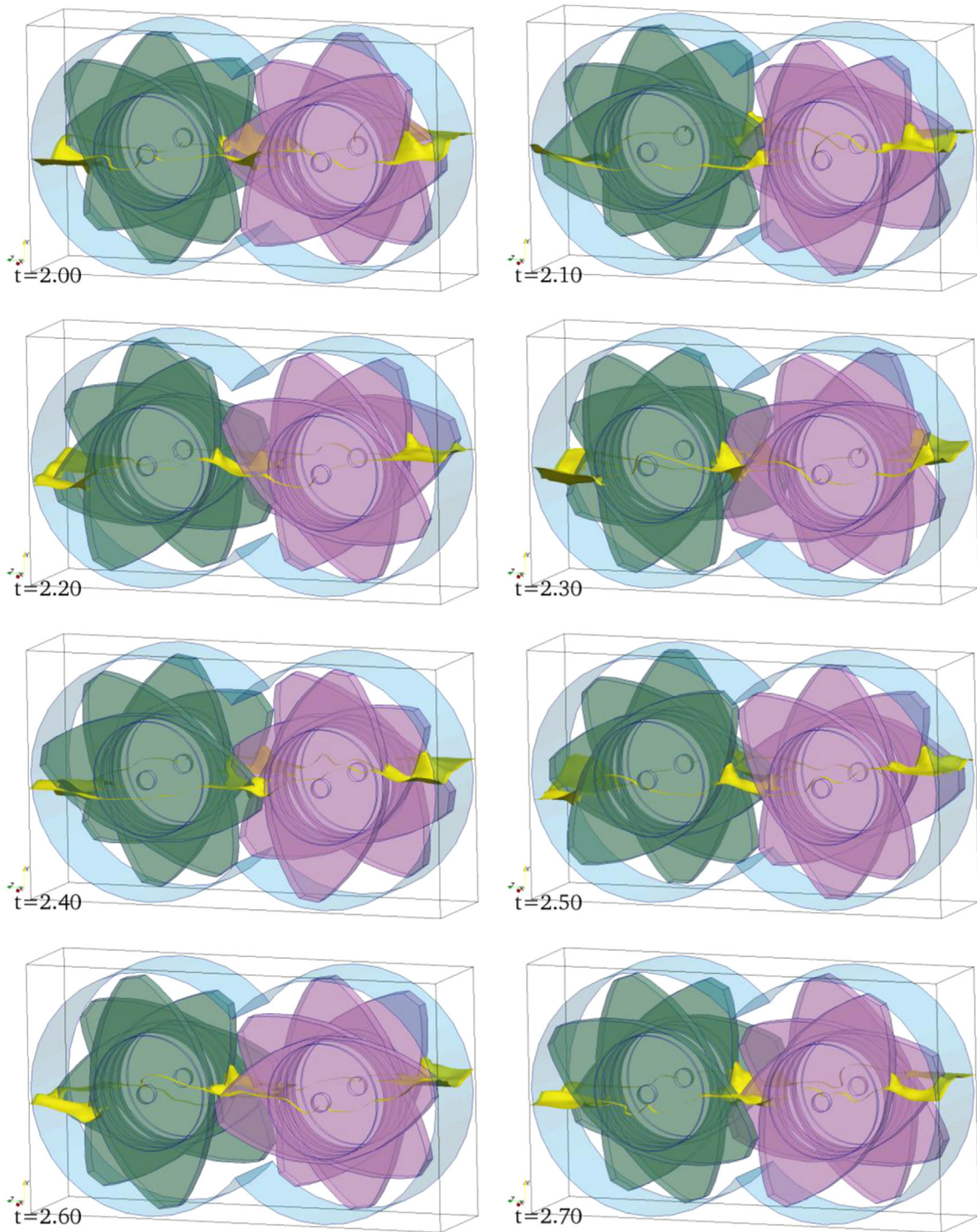


Fig. 19. Water surface during one period of TSK rotation.

hits the wall ($t=0.4$ s), a portion of air is trapped in the space enclosed by the water layer, tank and obstacle. As the water attached to the wall starts to fall ($t=0.5$ s), the air cushion is pushed to the obstacle side and tries to break through the water layer. At the same time, a secondary water tip penetrates into the air region. The computational results are likely to recover those interesting features in the experimental flow qualitatively.

7.3. Application to twin screw kneader (TSK)

In order to show the capability of the present method to model systems with extreme complexity, we present its application to 3D numerical simulations of a twin screw kneader (TSK). Nowadays

the TSK plays a primary role in the chemical industry including processes of compounding and mixing. Calculating flow patterns in a TSK is not easy for its geometrical complexity. In the past, the single-phase flow pattern in TSK has been studied numerically by using body-fitted meshes with grid super-imposition techniques provided in commercial packages, see e.g. (Jaffer et al., 2000; Nakayama et al., 2011; Wei et al., 2013; Zhang et al., 2009). To the best of our knowledge, the authors are not aware of any fixed grid-based TSK simulations taking account of the free surface motion.

In this study, such a case is carried out for our laboratory TSK system as illustrated in Fig. 17. The TSK has a sealed barrel and two screw elements that co-rotate in a counter-clockwise direction.

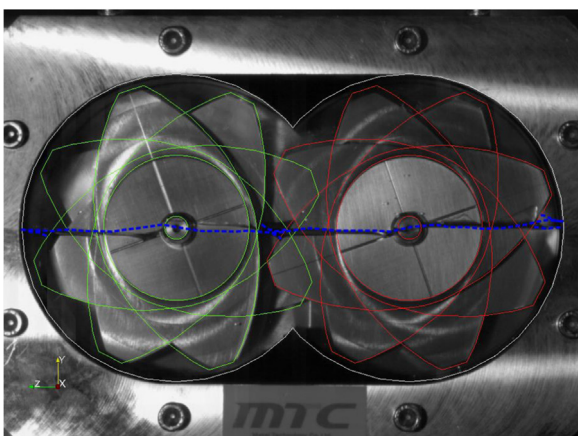
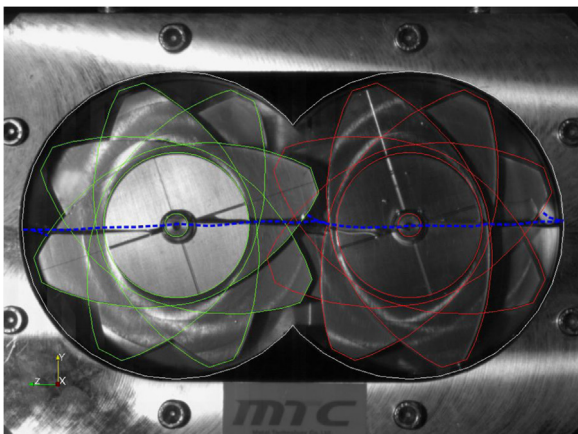


Fig. 20. Comparison of interface shapes with rotation speed of 30 rpm. The time interval between the two images is approximately 1/4 rotation period. The blue dashed line shows a sketch of computed results. (For interpretation of the references to color in this figure legend, the reader is referred to the web version of this article.)

The x -width (axial), y -height (vertical) and z -length (horizontal) of the outer barrel are 44 mm, 106 mm and 186 mm, respectively. A single screw paddle is composed of four oblique disks arranged in a whorl with 45° advance angle. A disk is 7 mm thick and the gap between two adjacent disks is about 3 mm. The screws outer diameter is 100 mm and the root diameter is approximately 50 mm. The center distance between the twin axes is equal to 80 mm. All the TSK parts, including the barrel and twin screws, are tackled by the SDF model and the IB method. Unlike some primary shapes (e.g. spheres and cylinders) that are often discussed in past IB literatures, it is almost impossible to represent the current TSK geometry in a trivial way. This point highlights the good applicability and flexibility of our modeling for arbitrarily shaped boundaries.

For the initial setup, water level is set to half the barrel height. Fluid density, dynamic viscosity and surface tension are set close to the physical properties of water and air under room temperature. The grid size is decided so that there is at least one fluid point in the narrow gap between two adjacent disks. The dilation approach introduced in Section 5.3 is used to treat the contact angle because boundaries can come very close in this problem. Three simulation cases with screw speeds of $\Omega=30$ rpm, 60 rpm and 90 rpm are considered in order to examine the effect of rotation speed. These computational conditions are summarized in Table 4. For this problem, the Reynolds number based on the tip speed U , disk cross-sectional length L and water kinematic viscosity ν is roughly estimated to be $Re \sim 5000$. In this study, turbulence models are not taken into

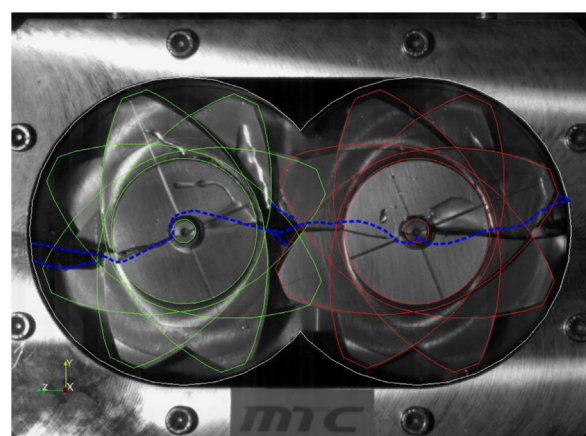
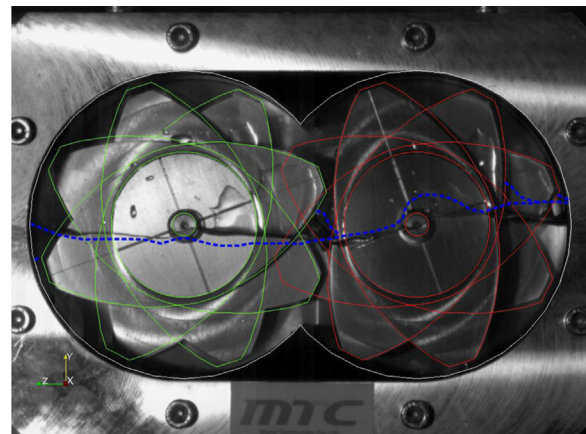


Fig. 21. Comparison of interface shapes with rotation speed of 90 rpm. The time interval between the two images is approximately 1/4 rotation period. The blue dashed line shows a sketch of computed results. (For interpretation of the references to color in this figure legend, the reader is referred to the web version of this article.)

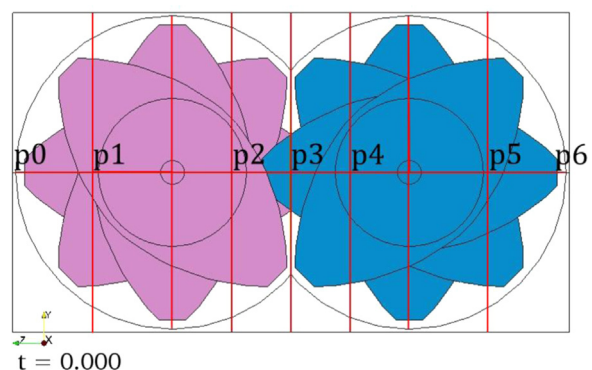


Fig. 22. Gauge positions for interface height measurement.

Table 5

Gauge positions for interface height measurement.

Gauge name	Gauge position
P0	Left wall
P1	Midpoint between left wall and left screw axis
P2	Midpoint between left screw axis and TSK center
P3	TSK center
P4	Midpoint between TSK center and right screw axis
P5	Midpoint between right screw axis and right wall
P6	Right wall

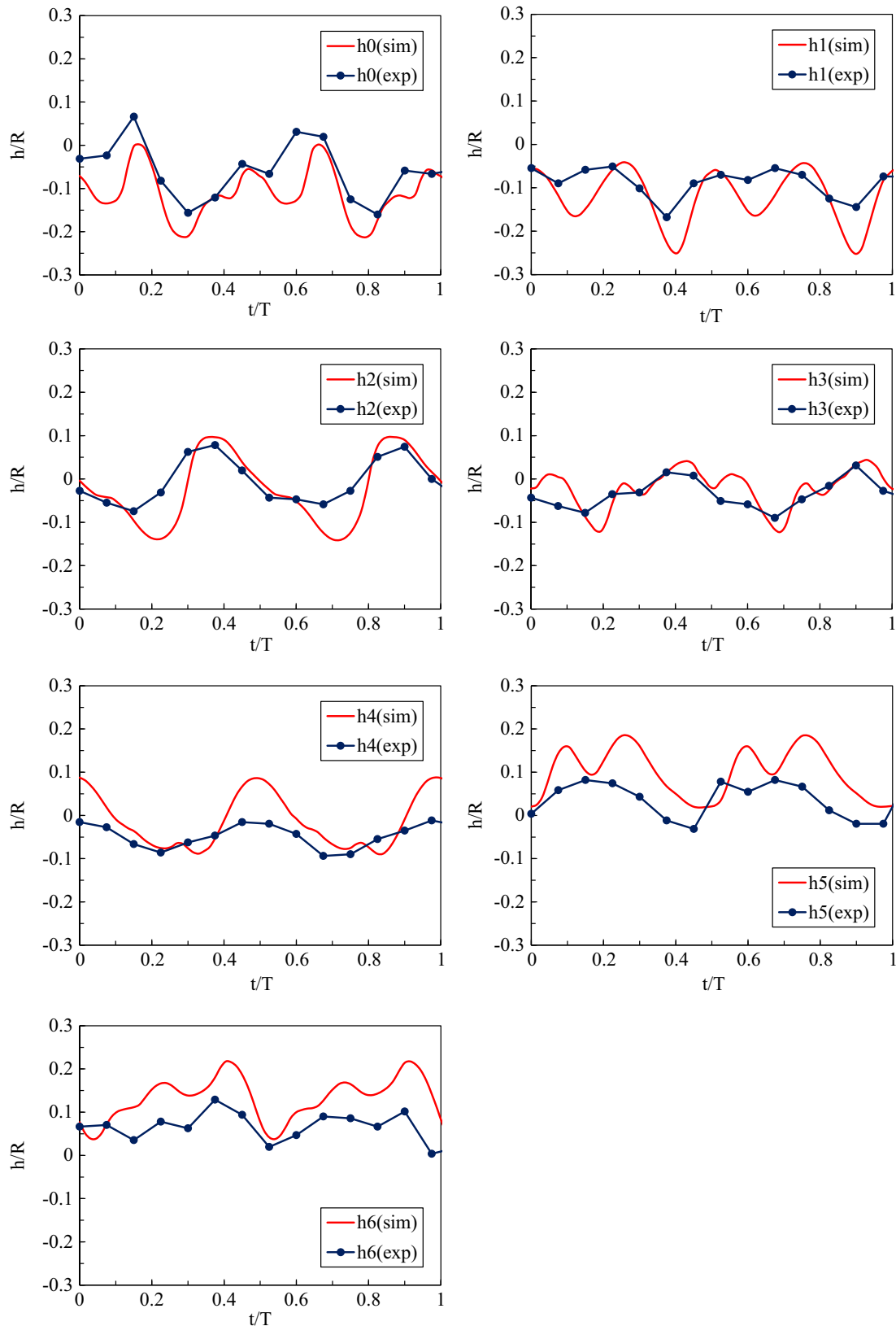


Fig. 23. The normalized water level at gauge positions P0–P6.

account because of the complex wall shapes; the LES approach suggested by (Yang and Stern, 2009) may be considered in the future.

We first present charts of the kinetic energy of the two-phase flow within the TSK as a function of time to depict the temporal evolvement of the system. Fig. 18(a) plots the kinetic energy per unit fluid volume e against simulation time t to show the

convergence towards quasi-steady states. From Fig. 18(a) it is seen that the air-water mixture starts with a state of rest and reaches the quasi-steady state very soon under the agitation of screw paddles in all cases. We have also noticed that, the relationship between temporal variation of kinetic energy and rotation speed can be more clearly revealed by plotting the normalized kinetic energy density $e^* = e/(\rho_m U^2/2)$ against the non-dimensional time $t^* = t/T$. Herein, ρ_m is the average fluid density which is equal to $\rho_m = 500.5 \text{ kg/m}^3$ in the current TSK system and $T = 60/\Omega$ is the rotation period of the screw paddles. This relationship is shown in Fig. 18(b) from which the flows in all three cases are known to reach quasi-steady states readily after one cycle of screw rotation, i.e. $t^* > 1$. After that, it seems that all simulation cases are shifted to a constant value of normalized kinetic energy density which is almost independent of the rotation speed. In the following sections, quasi-steady solutions of the TSK two-phase flow will be chosen from numerical results with simulation time $t > 2.0 \text{ s}$.

Next for one to have an image of the flow behavior inside the TSK system, Fig. 19 displays the configuration of the water surface during one single rotation of Case 3 with the largest rotation speed. As the screw disks periodically cut into and emerge from the water, they bring the fluid interface into motion and surface waves travel between two paddles. The water level in the right barrel is slightly higher than that in the left, due to the rotation direction. Those results seem reasonable. Again, we note that no re-gridding procedure is needed in this simulation.

In order to validate the simulations and demonstrate the effect of screw rotation, calculated results of Case 1 (30 rpm, the lowest rotation speed) and Case 3 (90 rpm, the highest rotation speed) are compared with experimental photographs taken by a high-speed camera. Fig. 20 shows such comparisons of interface shapes for Case 1 (30 rpm) where the background image is experimental photograph and the blue line is a sketch of simulation result. The time interval between Fig. 20(a) and (b) is a quarter of one rotation period. It is observed that the water surface remains almost flat in both simulation and experiment for the current rotation speed. On the other hand, the disturbance of fluid interface is rather obvious for Case 3 (90 rpm) as shown by Fig. 21. In Fig. 21(a) the water level is ascending from the left to the right side of the TSK and some liquid near the central part is attached to the left paddle exiting the water, which have been satisfactorily recovered by simulation results. In Fig. 21(b) the water level is higher in the middle part than other places. This is also captured by the simulation, except for that the height at the right wall is slightly overpredicted. The air cavity entrained behind the left paddle entering the water is confirmed as well. Therefore, the simulation results are found in qualitative agreement with validation data, showing that the VOF-IB method is able to correctly reflect the influence of different rotation speeds on two-phase agitation.

Finally, to further examine and validate the simulation of energetic fluid-boundary interactions in Case 3 (90 rpm), the comparison of interface heights at the TSK front wall is carried out for seven gauge positions, named from P0 to P6 respectively, whose locations are elucidated in Fig. 22 and Table 5. The horizontal line connecting the twin screw axes is chosen as the zero water level. The remainder fluctuation of the water height around the baseline is normalized by the radius of the TSK barrel. We note that experimental data is directly measured from the photographs because it is not realistic to install probes or sensors inside the TSK device. The series of water levels at different gauge positions are plotted against time in Fig. 23. Remarkable matches are found between the simulation and experiment in respects of the overall fluctuation pattern and oscillation frequency. However, it seems that the calculated wave motions generally have greater amplitude than those measured. For example, the left gauges (P0, P1 and P2) tend to be lower than their experimental counterparts whereas

the right ones (P4, P5 and P6) are slightly higher. It is possibly explained by that the boundary layer is artificially thickened by the IB model and thus more liquid has been transported to the right barrel. In the near future, we are planning a validation of the TSK simulation by using the particle image velocimetry (PIV) technique for detailed comparison of flow velocity fields.

The current TSK simulation is performed on a Windows PC equipped with Intel Core i7-3960X CPU, 3.3 GHz clock rate. The computation is parallelized on twelve threads and it takes 4.4 h of CPU time finish one TSK case of 4.0 s of real time.

8. Conclusions

In this study, we develop a numerical method for three-dimensional simulation of two-phase flows in complex geometries. The overall algorithm is based on the VOF method for two-phase flows and the IB modeling of wall boundaries. The shape and movement of general geometries are represented by an auxiliary SDF with local coordinate transformation. Numerical schemes are presented in detail to solve the interface advection, incompressible fluid dynamics, and the interaction with walls and moving objects. In addition, we describe simple ways to satisfy the neutral contact angle boundary condition on general geometries.

Various numerical tests have been performed to validate the present method. They contain steady flow driven by moving boundaries (concave surface in rotating barrel) and violent air-water flow interacting with rigid objects (dam break with an obstacle). Finally, the VOF-IB method is applied to the numerical simulation of the gas-liquid flow in a TSK, which is a very challenging problem featuring complicated interactions between two-phase flow and boundary with arbitrary shapes and movements. We have obtained reasonable predictions of this system in qualitative agreement with experimental validations. Hence, the VOF-IB method developed in this study is shown to be suitable for simulating two-phase flows in complex geometries. Its future extension will be combined with our recent granular flow modeling (Sun and Sakai, 2015) to simulate the gas-solid-liquid three-phase flows in TSK systems.

Acknowledgments

This study was supported by the Japan Society for the Promotion of Science (JSPS) KAKENHI Grant Number 13J09948. We are grateful to Prof. S. Koshizuka (The University of Tokyo) who has generously made available the photographs of dam break experiments. Kurimoto, Ltd. and Metal Technology Co. Ltd. are acknowledged for designing and providing the laboratory TSK device used in this study. We thank Dr. Y. Shigeto for his outstanding work on the SDF model. The first author would like to thank Dr. G. Basinskas and Mr. K. Takabatake from the University of Tokyo for the help with TSK experiments.

References

- Aniszewski, W., Ménard, T., Marek, M., 2014. Volume of Fluid (VOF) type advection methods in two-phase flow: a comparative study. *Comput. Fluids* 97, 52–73. <http://dx.doi.org/10.1016/j.compfluid.2014.03.027>.
- Arienti, M., Sussman, M., 2014. An embedded level set method for sharp-interface multiphase simulations of diesel injectors. *Int. J. Multiph. Flow* 59, 1–14. <http://dx.doi.org/10.1016/j.ijmultiphaseflow.2013.10.005>.
- Baltussen, M.W., Kuipers, J.A.M., Deen, N.G., 2014. A critical comparison of surface tension models for the volume of fluid method. *Chem. Eng. Sci.* 109, 65–74. <http://dx.doi.org/10.1016/j.ces.2013.12.045>.

- Barailler, F., Heniche, M., Tanguy, P.A., 2006. CFD analysis of a rotor-stator mixer with viscous fluids. *Chem. Eng. Sci.* 61, 2888–2894. <http://dx.doi.org/10.1016/j.ces.2005.10.064>.
- Brackbill, J., Kothe, D., Zemach, C., 1992. A continuum method for modeling surface tension. *J. Comput. Phys.* 100, 335–354. [http://dx.doi.org/10.1016/0021-9991\(92\)90240-Y](http://dx.doi.org/10.1016/0021-9991(92)90240-Y).
- Bunner, B., Tryggvason, G., 2002. Dynamics of homogeneous bubbly flows part 1. Rise velocity and microstructure of the bubbles. *J. Fluid Mech.* 466, 17–52. <http://dx.doi.org/10.1017/S0022112002001179>.
- Choi, J.I., Oberoi, R.C., Edwards, J.R., Rosati, J.A., 2007. An immersed boundary method for complex incompressible flows. *J. Comput. Phys.* 224, 757–784. <http://dx.doi.org/10.1016/j.jcp.2006.10.032>.
- Cundall, P.A., Strack, O.D.L., 1979. A discrete numerical model for granular assemblies. *Géotechnique* 29, 47–65. <http://dx.doi.org/10.1680/geot.1979.29.1.47>.
- Davanlou, A., Lee, J.D., Basu, S., Kumar, R., 2015. Effect of viscosity and surface tension on breakup and coalescence of bicomponent sprays. *Chem. Eng. Sci.* 131, 243–255. <http://dx.doi.org/10.1016/j.ces.2015.03.057>.
- Deen, N.G., Kuipers, J.A.M., 2013. Direct numerical simulation of wall-to liquid heat transfer in dispersed gas–liquid two-phase flow using a volume of fluid approach. *Chem. Eng. Sci.* 102, 268–282. <http://dx.doi.org/10.1016/j.ces.2013.08.025>.
- Deen, N.G., Van Sint Annaland, M., Kuipers, J.A.M., 2006. Direct numerical simulation of particle mixing in dispersed gas–liquid–solid flows using a combined volume of fluid and discrete particle approach, in: Proceedings of the Fifth International Conference on CFD in the Process Industries. Melbourne, Australia.
- Fadlun, E.A., Verzicco, R., Orlandi, P., Mohd-Yusof, J., 2000. Combined Immersed-boundary finite-difference methods for three-dimensional complex flow simulations. *J. Comput. Phys.* 161, 35–60. <http://dx.doi.org/10.1006/jcph.2000.6484>.
- Francois, M.M., Cummins, S.J., Dendy, E.D., Kothe, D.B., Sicilian, J.M., Williams, M.W., 2006. A balanced-force algorithm for continuous and sharp interfacial surface tension models within a volume tracking framework. *J. Comput. Phys.* 213, 141–173. <http://dx.doi.org/10.1016/j.jcp.2005.08.004>.
- Fujita, M., Koike, O., Yamaguchi, Y., 2015. Direct simulation of drying colloidal suspension on substrate using immersed free surface model. *J. Comput. Phys.* 281, 421–448. <http://dx.doi.org/10.1016/j.jcp.2014.10.042>.
- Ge, Y., Fan, L.S., 2006. 3-D direct numerical simulation of gas–liquid and gas–liquid–solid flow systems using the level-set and immersed boundary methods. *Adv. Chem. Eng.* 31, 1–63. [http://dx.doi.org/10.1016/S0065-2377\(06\)31001-0](http://dx.doi.org/10.1016/S0065-2377(06)31001-0).
- Gopala, V.R., van Wachem, B.G.M., 2008. Volume of fluid methods for immiscible-fluid and free-surface flows. *Chem. Eng. J.* 141, 204–221.
- Gueyffier, D., Li, J., Nadim, A., Scardovelli, R., Zaleski, S., 1999. Volume-of-fluid interface tracking with smoothed surface stress methods for three-dimensional flows. *J. Comput. Phys.* 152, 423–456.
- Hirt, C., Nichols, B., 1981. Volume of fluid (VOF) method for the dynamics of free boundaries. *J. Comput. Phys.* 39, 201–225.
- Homma, S., Koga, J., Matsumoto, S., Song, M., Tryggvason, G., 2006. Breakup mode of an axisymmetric liquid jet injected into another immiscible liquid. *Chem. Eng. Sci.* 61, 3986–3996. <http://dx.doi.org/10.1016/j.ces.2006.01.029>.
- Ikeno, T., Kajishima, T., 2007. Finite-difference immersed boundary method consistent with wall conditions for incompressible turbulent flow simulations. *J. Comput. Phys.* 226, 1485–1508. <http://dx.doi.org/10.1016/j.jcp.2007.05.028>.
- Jaffer, S.A., Bravo, V.L., Wood, P.E., Hrymak, A.N., Wright, J.D., 2000. Experimental validation of numerical simulations of the kneading disc section in a twin screw extruder. *Polym. Eng. Sci.* 40, 892–901. <http://dx.doi.org/10.1002/pen.11217>.
- Jain, D., Deen, N.G., Kuipers, J.A.M., Antonyuk, S., Heinrich, S., 2012. Direct numerical simulation of particle impact on thin liquid films using a combined volume of fluid and immersed boundary method. *Chem. Eng. Sci.* 69, 530–540. <http://dx.doi.org/10.1016/j.ces.2011.11.018>.
- Jain, D., Kuipers, J.A.M., Deen, N.G., 2014. Numerical study of coalescence and breakup in a bubble column using a hybrid volume of fluid and discrete bubble model approach. *Chem. Eng. Sci.* 119, 134–146. <http://dx.doi.org/10.1016/j.ces.2014.08.026>.
- Kajishima, T., Takiguchi, S., 2002. Interaction between particle clusters and particle-induced turbulence. *Int. J. Heat Fluid Flow* 23, 639–646. [http://dx.doi.org/10.1016/S0142-727X\(02\)00159-5](http://dx.doi.org/10.1016/S0142-727X(02)00159-5).
- Kajishima, T., Takiguchi, S., Hamasaki, H., Miyake, Y., 2001. Turbulence structure of particle-laden flow in a vertical plane channel due to vortex shedding. *JSME Int. J. Ser. B* 44, 526–535. <http://dx.doi.org/10.1299/jsmeb.44.526>.
- Kleefsman, K.M.T., Fekken, G., Veldman, A.E.P., Iwanowski, B., Buchner, B., 2005. A volume-of-fluid based simulation method for wave impact problems. *J. Comput. Phys.* 206, 363–393. <http://dx.doi.org/10.1016/j.jcp.2004.12.007>.
- Koshizuka, S., Tamako, H., Oka, Y., 1995. A particle method for incompressible viscous flow with fluid fragmentation. *Comput. Fluid Dyn. J.* 4, 29–46.
- Lin, P., 2007. A fixed-grid model for simulation of a moving body in free surface flows. *Comput. Fluids* 36, 549–561. <http://dx.doi.org/10.1016/j.compfluid.2006.03.004>.
- Lin, S.Y., Chen, Y.C., 2013. A pressure correction-volume of fluid method for simulations of fluid–particle interaction and impact problems. *Int. J. Multiph. Flow* 49, 31–48. <http://dx.doi.org/10.1016/j.ijmultiphaseflow.2012.09.003>.
- Lin, S.Y., Chin, Y.H., Hu, J.J., Chen, Y.C., 2011. A pressure correction method for fluid–particle interaction flow: direct-forcing method and sedimentation flow. *Int. J. Numer. Methods Fluids* 67, 1771–1798. <http://dx.doi.org/10.1002/fld.2442>.
- Ma, T., Lucas, D., Ziegenhein, T., Fröhlich, J., Deen, N.G., 2015. Scale-adaptive simulation of a square cross-sectional bubble column. *Chem. Eng. Sci.* 131, 101–108. <http://dx.doi.org/10.1016/j.ces.2015.03.047>.
- Mahulkar, A.V., Marin, G.B., Heynderickx, G.J., 2015. Droplet–wall interaction upon impingement of heavy hydrocarbon droplets on a heated wall. *Chem. Eng. Sci.* 130, 275–289. <http://dx.doi.org/10.1016/j.ces.2015.03.012>.
- Matsumoto, K., Ohta, M., Iwata, S., 2015. Numerical analysis of flow dynamics of milk in a milk-filling process. *Kagaku Kogaku Ronbunshu* 41, 1–10. <http://dx.doi.org/10.1252/kakoronbunshu.41.1>.
- Nabavi, S.A., Vladislavjević, G.T., Gu, S., Ekanem, E.E., 2015. Double emulsion production in glass capillary microfluidic device: parametric investigation of droplet generation behaviour. *Chem. Eng. Sci.* 130, 183–196. <http://dx.doi.org/10.1016/j.ces.2015.03.004>.
- Nakayama, Y., Takeda, E., Shigeishi, T., Tomiyama, H., Kajiwara, T., 2011. Melt-mixing by novel pitched-tip kneading disks in a co-rotating twin-screw extruder. *Chem. Eng. Sci.* 66, 103–110. <http://dx.doi.org/10.1016/j.ces.2010.10.022>.
- Noh, W.F., Woodward, P., 1976. Some methods of resolution of free surface problems, lecture notes in physics, in: Proceedings of the Fifth International Conference on Numerical Methods in Fluid Dynamics, June 28–July 2, 1976 Twente University, Enschede. Springer Berlin Heidelberg, Berlin, Heidelberg. doi:10.1007/3-540-08004-X.
- Osher, S., Fedkiw, R., 2002. *Level Set Methods and Dynamic Implicit Surfaces* (Google eBook). Springer, New York.
- Peskin, C.S., 2002. The immersed boundary method. *Acta Numer.* 11, 479–517. <http://dx.doi.org/10.1017/S0962492902000077>.
- Peskin, C.S., 1977. Numerical analysis of blood flow in the heart. *J. Comput. Phys.* 25, 220–252. [http://dx.doi.org/10.1016/0021-9991\(77\)90100-0](http://dx.doi.org/10.1016/0021-9991(77)90100-0).
- Rider, W.J., Kothe, D.B., 1998. Reconstructing volume tracking. *J. Comput. Phys.* 141, 112–152. <http://dx.doi.org/10.1006/jcph.1998.5906>.
- Santana, H.S., Silva, J.L., Taranto, O.P., 2015. Numerical simulation of mixing and reaction of Jatropha curcas oil and ethanol for synthesis of biodiesel in micromixers. *Chem. Eng. Sci.* 132, 159–168. <http://dx.doi.org/10.1016/j.ces.2015.04.014>.
- Seo, J.H., Mittal, R., 2011. A sharp-interface immersed boundary method with improved mass conservation and reduced spurious pressure oscillations. *J. Comput. Phys.* 230, 7347–7363. <http://dx.doi.org/10.1016/j.jcp.2011.06.003>.
- Shigeto, Y., Sakai, M., 2013. Arbitrary-shaped wall boundary modeling based on signed distance functions for granular flow simulations. *Chem. Eng. J.* 231, 464–476.
- Solsvik, J., Jakobsen, H.A., 2015. Single drop breakup experiments in stirred liquid–liquid tank. *Chem. Eng. Sci.* 131, 219–234. <http://dx.doi.org/10.1016/j.ces.2015.03.059>.
- Son, G., 2005. A level set method for incompressible two-fluid flows with immersed solid boundaries. *Numer. Heat Transf. Part B Fundam.* 47, 473–489. <http://dx.doi.org/10.1080/10407790590919252>.
- Spalding, D.B., 1972. A novel finite difference formulation for differential expressions involving both first and second derivatives. *Int. J. Numer. Methods Eng.* 4, 551–559. <http://dx.doi.org/10.1002/nme.1620040409>.
- Sun, X., Sakai, M., 2015. Three-dimensional simulation of gas–solid–liquid flows using the DEM–VOF method. *Chem. Eng. Sci.* 134, 531–548. <http://dx.doi.org/10.1016/j.ces.2015.05.059>.
- Sun, X., Sakai, M., Sakai, M.-T., Yamada, Y., 2014. A Lagrangian–Lagrangian coupled method for three-dimensional solid–liquid flows involving free surfaces in a rotating cylindrical tank. *Chem. Eng. J.* 246, 122–141. <http://dx.doi.org/10.1016/j.cej.2014.02.049>.
- Sun, X., Sakai, M., Yamada, Y., 2013. Three-dimensional simulation of a solid–liquid flow by the DEM–SPH method. *J. Comput. Phys.* 248, 147–176. <http://dx.doi.org/10.1016/j.jcp.2013.04.019>.
- Sussman, M., 2005. A parallelized, adaptive algorithm for multiphase flows in general geometries. *Comput. Struct.* 83, 435–444. <http://dx.doi.org/10.1016/j.compstruc.2004.06.006>.
- Sussman, M., 2001. An adaptive mesh algorithm for free surface flows in general geometries. In: Vande Wouwer, A., Saucier, P., Schiesser, W. (Eds.), *Adaptive Method of Lines*. Chapman and Hall/CRC, USA.
- Sussman, M., Fatemi, E., Smereka, P., Osher, S., 1998. An improved level set method for incompressible two-phase flows. *Comput. Fluids* 27, 663–680.
- Sussman, M., Ohta, M., 2009. A stable and efficient method for treating surface tension in incompressible two-phase flow. *SIAM J. Sci. Comput.* 31, 2447–2471. <http://dx.doi.org/10.1137/080732122>.
- Sussman, M., Puckett, E.G., 2000. A coupled level set and volume-of-fluid method for computing 3D and Axisymmetric incompressible two-phase flows. *J. Comput. Phys.* 162, 301–337.
- Sussman, M., Smereka, P., Osher, S., 1994. A level set approach for computing solutions to incompressible two-phase flow. *J. Comput. Phys.* 114, 146–159.
- Tryggvason, G., Scardovelli, R., Zaleski, S., 2011. *Direct Numerical Simulations of Gas–Liquid Multiphase Flows*, 1st ed. Cambridge University Press, New York.
- Uhlmann, M., 2005. An immersed boundary method with direct forcing for the simulation of particulate flows. *J. Comput. Phys.* 209, 448–476. <http://dx.doi.org/10.1016/j.jcp.2005.03.017>.
- Van Sint Annaland, M., Deen, N.G., Kuipers, J.A.M., 2005. Numerical simulation of gas bubbles behaviour using a three-dimensional volume of fluid method. *Chem. Eng. Sci.* 60, 2999–3011. <http://dx.doi.org/10.1016/j.ces.2005.01.031>.
- Wang, X., Zhu, C., Wu, Y., Fu, T., Ma, Y., 2015. Dynamics of bubble breakup with partly obstruction in a microfluidic T-junction. *Chem. Eng. Sci.* 132, 128–138. <http://dx.doi.org/10.1016/j.ces.2015.04.038>.

- Wei, J., Liang, XL., Chen, DB., Yang, YL., Zhou, D.M., 2014. Evaluation of the mixing performance for one novel twin screw kneader with particle tracking. *Polym Eng Sci* 54, 2407–2419. <http://dx.doi.org/10.1002/pen.23786>.
- Yabe, T., Chinda, K., Hiraishi, T., 2007. Computation of surface tension and contact angle and its application to water strider. *Comput. Fluids* 36, 184–190. <http://dx.doi.org/10.1016/j.compfluid.2005.07.011>.
- Yamada, Y., Sakai, M., 2013. Lagrangian-Lagrangian simulations of solid-liquid flows in a bead mill. *Powder Technol.* 239, 105–114. <http://dx.doi.org/10.1016/j.powtec.2013.01.030>.
- Yang, J., Balaras, E., 2006. An embedded-boundary formulation for large-eddy simulation of turbulent flows interacting with moving boundaries. *J. Comput. Phys.* 215, 12–40. <http://dx.doi.org/10.1016/j.jcp.2005.10.035>.
- Yang, J., Stern, F., 2009. Sharp interface immersed-boundary/level-set method for wave-body interactions. *J. Comput. Phys.* 228, 6590–6616. <http://dx.doi.org/10.1016/j.jcp.2009.05.047>.
- Yokoi, K., 2013. A practical numerical framework for free surface flows based on CLSVOF method, multi-moment methods and density-scaled CSF model: numerical simulations of droplet splashing. *J. Comput. Phys.* 232, 252–271. <http://dx.doi.org/10.1016/j.jcp.2012.08.034>.
- Yokoi, K., 2007. Efficient implementation of THINC scheme: a simple and practical smoothed VOF algorithm. *J. Comput. Phys.* 226, 1985–2002.
- Yoon, H.S., Jeon, C.H., Jung, J.H., Koo, B., Choi, C., Shin, S.C., 2013. Simulation of two-phase flow-body interaction problems using direct forcing/fictitious domain-level set method. *Int. J. Numer. Methods Fluids* 73, 250–265. <http://dx.doi.org/10.1002/fld.3797>.
- Youngs, D.L., 1982. Time-dependent multi-material flow with large fluid distortion. *Numer. Methods Fluid Dyn.* 24, 273–285.
- Zalesak, S.T., 1979. Fully multidimensional flux-corrected transport algorithms for fluids. *J. Comput. Phys.* 31, 335–362. [http://dx.doi.org/10.1016/0021-9991\(79\)90051-2](http://dx.doi.org/10.1016/0021-9991(79)90051-2).
- Zhang, X.M., Feng, L.F., Chen, W.X., Hu, G.H., 2009. Numerical simulation and experimental validation of mixing performance of kneading discs in a twin screw extruder. *Polym. Eng. Sci.* 49, 1772–1783. <http://dx.doi.org/10.1002/pen.21404>.